Results in Engineering 32 (2026) 113345

Contents lists available at ScienceDirect

Results in Engineering

journal homepage: www.sciencedirect.com/journal/results-in-engineering

Research paper

Multiplexer microfluidic platform for mixing and driving Newtonian fluids under high flow rate ratios

Filipe Ferreira [a], Paulo J. Sousa [a,b], Graça Minas [a,b], Rui A. Lima [c,d,e], Vânia C. Pinto [a,b], Susana O. Catarino [a,b,*]

[a] Microelectromechanical Systems Research Unit (CMEMS), University of Minho, Guimarães, 4800-058, Portugal
[b] LABBELS – Associate Laboratory, University of Minho, Braga, 4710-057, Portugal
[c] Mechanical Engineering and Resource Sustainability Center (MEtRICs), Mechanical Engineering Department, University of Minho, Guimarães, 4800-058, Portugal
[d] Transport Phenomena Research Center (CEFT), Faculdade de Engenharia da Universidade do Porto (FEUP), Porto, 4200-465, Portugal
[e] Associate Laboratory in Chemical Engineering (ALiCE), Faculty of Engineering, University of Porto, Porto, 4200-465, Portugal

ARTICLE INFO

Keywords:
COMSOL multiphysics
Lab-on-a-chip
Microfluidics
Multiplexer
Numerical simulation
Passive micromixers

ABSTRACT

In recent years, microfluidics has contributed to the development of new solutions for the detection and monitoring of several diseases, through point-of-care (PoC) systems, which are simpler and cheaper than conventional detection methods. However, these systems still face some challenges, particularly when uniform mixing is required for biological and chemical reactions. Passive micromixers have emerged as a viable solution, as they are integrated into the microchannel geometry, requiring no external energy source and are simple to operate. Thus, this work focused on the design, development, numerical simulation and experimental characterizaton of polydimethylsiloxane (PDMS) multiplexer microfluidic devices for effective mixing and driving of fluids to three circular reaction chambers, under different flow ratios, making it possible the simultaneous quantification of three different analytes. Two configurations were considered for the passive micromixers: one based on a Tesla-type structure and the other incorporating a half-moon-shaped pattern implemented along a serpentine. Both geometries of the microdevice achieved uniform mixing of two fluids, under a laminar regime, and ensured equal transport of the mixed fluid (in fluid velocity and volume) to the chambers, at three flow ratios: 1:1, 1:3, and 1:6. The results of the experimental tests showed good agreement with 2D numerical simulations performed in COMSOL Multiphysics.

The developed platforms demonstrate an effective proof of concept for future integration within a microfluidic biosensing platform, enabling the simultaneous detection and monitoring of multiple biomarkers and contributing to the advancement of compact and efficient PoC diagnostic systems.

1. Introduction

Microfluidics has recently emerged with enormous potential to revolutionize point-of-care (PoC) diagnostics, as it allows the study and manipulation of fluids at the microscale through the geometric miniaturization of devices comprising channels and/or reaction chambers with dimensions in the order of micrometers [1–4]. For this reason, reagent consumption is drastically lower than conventional macroscale methods, resulting in reduced per test and device costs, as well as portability due to the reduced size. In addition, a microfluidic platform allows parallelization, i.e., the possibility of performing different tests for several purposes on a single chip at the same time, resulting in reduced processing time with high precision [5–8].

Due to the small size of the microfluidic channels and, assuming Newtonian fluids (with constant viscosity), the flow regime in microfluidic platforms is laminar, with viscous forces dominating over inertial forces, resulting in predominantly diffusive transport of species and potentially slower mixing processes. This fact is proven by Reynolds' Eq. (1) [9–11]:

$$Re = \frac{\rho U l}{\mu} = \frac{inertial\ forces}{viscous\ forces} \quad (1)$$

where Re is the dimensionless Reynolds number (a flow is considered laminar for $Re < 2000$ and turbulent for $Re > 2000$), ρ the density of the

* Corresponding author at: Microelectromechanical Systems Research Unit (CMEMS), University of Minho, 4800-058 Guimarães, Portugal.
E-mail address: scatarino@dei.uminho.pt (S.O. Catarino).

https://doi.org/10.1016/j.rineng.2026.113345
Received 9 March 2026; Received in revised form 11 September 2026; Accepted 2 October 2026
Available online 3 October 2026
2590-1230/© 2026 The Authors. Published by Elsevier B.V. This is an open access article under the CC BY-NC license (http://creativecommons.org/licenses/by-nc/4.0/).

fluid (kg/m^3), U the flow velocity (m/s), l the characteristic width of the flow (e.g., microchannel width), and μ the dynamic viscosity of the fluid (Pa·s) [12,13]. In microfluidic structures with characteristic dimensions in the micrometer range, the *Re* is typically very low, often much less than 1. Likewise, the Péclet number (*Pe*) is a dimensionless number relevant in the context of microfluidic dynamics, expressing the ratio between advective and diffusive transport of species, as described in Equation 2 [14–16]:

$$Pe = \frac{l^2/D}{l/U} = \frac{t_{diffusion}}{\tau_{advection}} = \frac{lU}{D} = \frac{advective\ transport}{diffusive\ transport} \quad (2)$$

where D (m^2/s) is the characteristic diffusion coefficient of the species (indicating the substance's ability to diffuse in the medium with variations from 10×10^{-9} m^2/s for ions to 10×10^{-14} m^2/s for larger cells or biomolecules), $t_{diffusion}$ corresponds to the time of diffusive transport and $\tau_{advection}$ to the time of advective transport [17]. Again, the small dimensions of microchannels result in low *Pe* values (typically < 10), turning diffusion the dominant transport mechanism, while advection can be neglected [18,19].

Consequently, in a diffusion-based mixing process, both the mixing time and efficiency depend on increasing the interfacial contact between particles, both through active and passive methods [20]. In active micromixers, mixing is promoted by external energy sources - electric or magnetic fields, acoustic, thermal, among others - that are applied through a specific transducer [21–24]. However, these external factors can affect the intrinsic properties of the samples (such as deformability or mechanical integrity) and are substantially more expensive and complex due to the need for additional equipment [25–27].

In contrast, passive micromixers rely solely on the manipulation of the microchannel geometry and on the control of flow conditions to maximize fluid interaction, by increasing the fluids' travelling time and the contact area between the species, without external actuation [28]. These strategies induce mixing through mechanisms of flux splitting-recombination, vortices or fluid collisions along the channel [29–31]. Several geometric configurations have been proposed, such as lamination, serpentines, "zigzag" structures and inner obstacles, enhancing the interaction between the fluids and promoting chaotic advection through inertial forces [32–36]. Owing to their simplicity, low fabrication costs and ease of integration into microfluidic platforms, the passive micromixers have been widely adopted [37,38].

In parallel, multiplexing microfluidics devices have attracted considerable attention due to their ability to simultaneously distribute samples and reagents to multiple reaction sites, enabling high-throughput and parallelized analyses. These devices have been recently reported for several (bio)medical, environmental or biochemical applications. Specifically, multiplexer microfluidics has been employed for simultaneous biosensing in health monitoring [39], cancer biomarkers detection [40], respiratory pathogens detection [41], drinking water monitoring (e.g., heavy metals and nutrients) [42], food safety assessment (e.g., foodborne bacteria) [43], and nucleic acid analysis (e.g., Deoxyribonucleic acid (DNA), exosomal micro ribonucleic acid (miRNA) and pathogen ribosomal ribonucleic acid (rRNA)) [44–46].

However, the integration of efficient passive mixing with homogeneous flow distribution remains a significant challenge for further implementation in PoC systems. For the simultaneous detection of different biomarkers within the same microfluidic platform, not only is the uniform mixing of samples and reagents crucial, but also the equal distribution of the mixed fluid among multiple detection chambers. Although many multiplexer microfluidic systems have been reported in the literature, many of these are active systems, i.e., require external pumping or actuation equipment, which may increase system complexity and cost. Additionally, quantitative assessment of mixing efficiency and fluid distribution remain limited on these devices. To the best of the authors' knowledge, no current research has fully reported the optimization of passive multiplexer devices capable of, simultaneously, efficiently ensuring the mixing of samples under different flow rates, while guaranteeing their equitable arrival, regarding fluid velocity and volume, across three parallel reaction chambers. Therefore, this

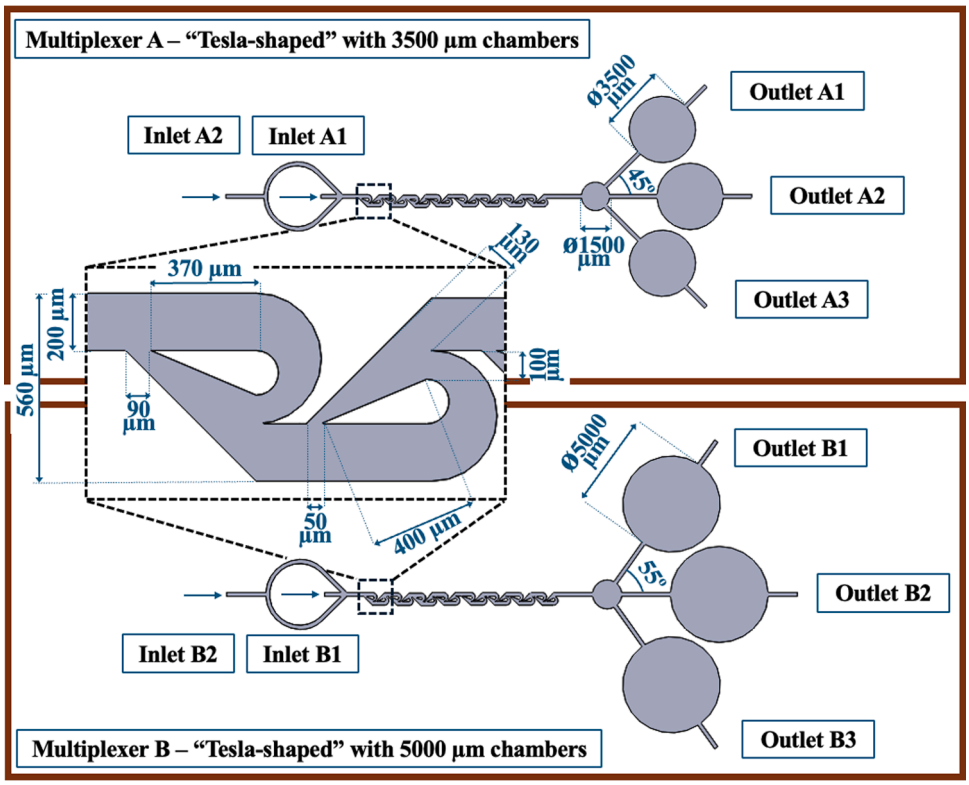


Fig. 1. Schematic diagram illustrating the geometries and dimensions of the "Tesla-shaped" multiplexers.

work focused on the development and comparison between two microfluidic multiplexer platforms, both with a mixing region and three parallel reaction chambers, to ensure an efficiently passive mixing of samples (targeting mixing indices above 80%) under different flow rates (between 5 and 30 μL/min flow rate combinations), while guaranteeing their equitable arrival, regarding fluid velocity and volume (targeting volume uniformity with coefficient of variation (CV) below 10%), across three parallel millimetric reaction chambers. Furthermore, two different reaction chamber configurations (with 3500 μm and 5000 μm diameters) were investigated to evaluate the influence of the chamber diameter on mixing and fluid distribution. The design and dimension of these chambers took into account the goal of future integration of these microfluidic systems with automatic and miniaturized optical detection systems, comprising light emitting diodes – LEDs, photodiodes and similar components, which must fit and align with the chambers (as in [47,48]). For that purpose, a set of microdevices, fabricated in polydimethylsiloxane (PDMS), through a low-cost process of soft lithography and replica molding, were designed to operate under laminar conditions at three different flow ratios: 1:1, 1:3, and 1:6. Numerical simulations using COMSOL Multiphysics were also conducted to evaluate and predict mixing and transport efficiency, followed by experimental analysis.

2. Multiplexer design

The multiplexer devices comprise a passive mixing region to ensure efficient mixing between two fluids, followed by three reaction chambers for the further simultaneous detection of different biomarkers, and a compensation chamber, placed upstream of the three reaction chambers to stabilize the flow. In this work, four 2D multiplexer devices were investigated, combining two passive micromixers geometries already reported in the literature and adapted - namely, "Tesla-shaped" and "half-moon-shaped" – with two sets of reaction chambers with 3500 μm and 5000 μm diameters, respectively. All those geometries were designed in CAD (Computer-Aided Design) using SolidWorks, for further numerical analysis and device fabrication.

The "Tesla-shaped" micromixer, described by Hossain et al. [49], is based on a structure originally developed by Nikola Tesla, in which the flow follows chaotic advection, and then promotes the fluid mixing. The structure consists of a partial split of the flow at a channel constriction, increasing its velocity, while the remaining flux undergoes a vortex and emerges in the opposite direction, increasing species interaction. The design presented by the Hossain et al. [49], featuring a maximum channel width of 200 μm, was adapted by set the constriction width to

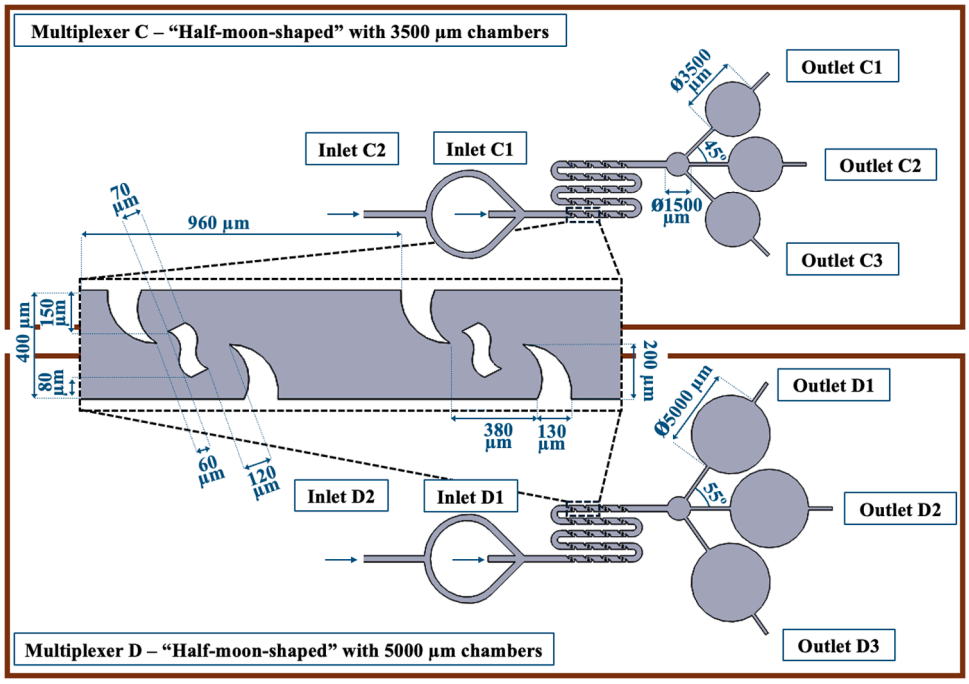


Fig. 2. Schematic diagram illustrating the geometries and dimensions of the "half-moon-shaped" multiplexers.

Table 1
Number of mesh elements and corresponding maximum velocity obtained for the different mesh refinement levels in each micromixer geometry.

	A – "Tesla-shaped" with 3500 μm chambers		D – "Tesla-shaped" with 5000 μm chambers		C – "Half-moon-shaped" with 3500 μm chambers		D – "Half-moon-shaped" with 5000 μm chambers	
Mesh Refinement	**Number of Elements**	**Maximum Velocity (m/s)**	**Number of Elements**	**Maximum Velocity (m/s)**	**Number of Elements**	**Maximum Velocity (m/s)**	**Number of Elements**	**Maximum Velocity (m/s)**
1. Extremely Coarse	4183	0.08048	3715	0.08543	5394	0.04619	4529	0.03874
2. Extra Coarse	5356	0.08597	4741	0.08605	7407	0.04862	6322	0.04717
3. Coarser	7397	0.09245	6628	0.09584	11019	0.05578	9950	0.04861
4. Coarse	11703	0.09959	9969	0.09596	19589	0.05943	15739	0.05569
5. Normal	14701	0.10076	15034	0.10168	32858	0.05943	29280	0.06582
6. Fine	21815	0.10134	22077	0.10065	46936	0.06975	47453	0.06915
7. Finer	30432	0.10595	31877	0.10292	59292	0.07194	59960	0.06915
8. Extra Fine	58704	0.11752	58604	0.11332	106533	0.07427	107011	0.07402
9. Extremely Fine	63708	0.11776	64352	0.11334	115139	0.07412	116061	0.07426

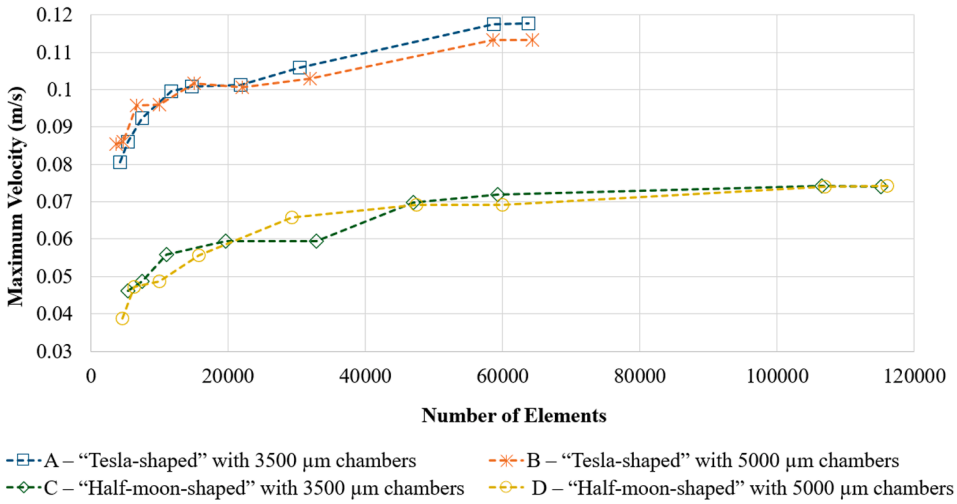


Fig. 3. Mesh independence study assessed by the maximum velocity (m/s) at different refinement levels for each geometry.

50 and 90 μm, respectively, and replicating the mixing unit eight times along the microchannel, as shown in Fig. 1. For a better identification of the "Tesla-shaped" microchannels' regions, in the multiplexer with 3500 μm diameter chambers, the inlets are labeled A1 and A2 and the outlets are labeled A1 to A3; in the multiplexer with 5000 μm diameter chambers, the inlets are labeled B1 and B2, and the outlets B1 to B3.

Similarly, the designated "half-moon-shaped" micromixer was adjusted from the o presented by Dehghani et al. [50], which is also based on chaotic advection and is composed of two semicircular half-moon structures implemented symmetrically on opposite walls and separated by a central obstacle that divides the flow. Subsequently, both flux streams undergo vortex formation and collide in opposite directions. The dimensions of the mixing structure were doubled from the original design reported by the Dehghani et al. [50], with a maximum channel width of 400 μm, as can be observed in Fig. 2. Additionally, the mixing unity was replicated four times along a serpentine channel with five segments to maximize the mixing efficiency. For a better identification of the "half-moon-shaped" microchannels' regions, in the multiplexer with 3500 μm diameter chambers, the inlets are labeled C1 and C2 and the outlets are labeled C1 to C3; in the multiplexer with 5000 μm diameter chambers, the inlets are labeled D1 and D2, and the outlets D1 to D3.

It is important to notice that, for both mixer designs, an inlet configuration strategy was adopted to prevent undesired flow reversal of fluid from Inlet 2 (subject to flow rate variations) into Inlet 1, even at higher flow ratio conditions.

3. Numerical simulation

The numerical study was implemented in COMSOL Multiphysics software, version 5.3, as it offers several predefined computational fluid dynamics (CFD) interfaces to solve the numerical model by finite element methods (FEM). In this study, two physical modules were implemented: laminar flow (1), which is the characteristic flow regime in microfluidic systems; and transport of diluted species (2), allowing the simulation of particles movement in microchannels by diffusion/advection.

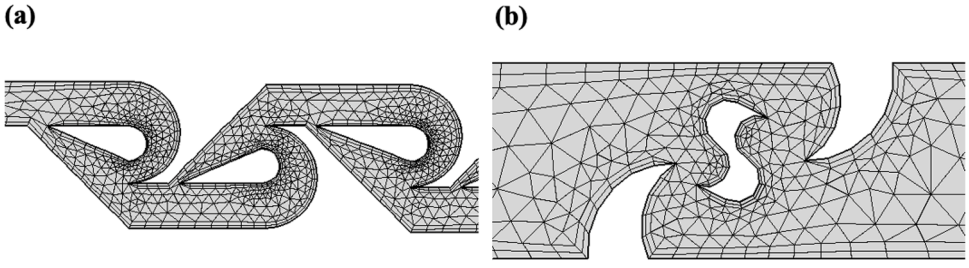


Fig. 4. Detail of the 2D meshes of the mixing structures in (a) "Tesla-shaped" and (b) "half-moon-shaped" multiplexers.

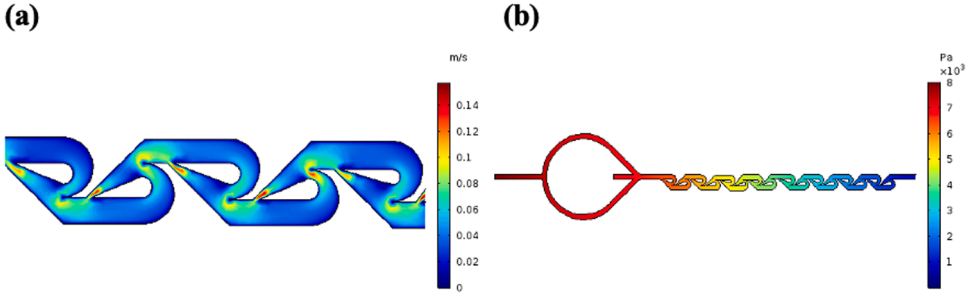


Fig. 5. Steady-state distribution of (a) velocity magnitude (m/s) and (b) pressure (Pa) in the mixing region of the "Tesla-shaped" multiplexer.

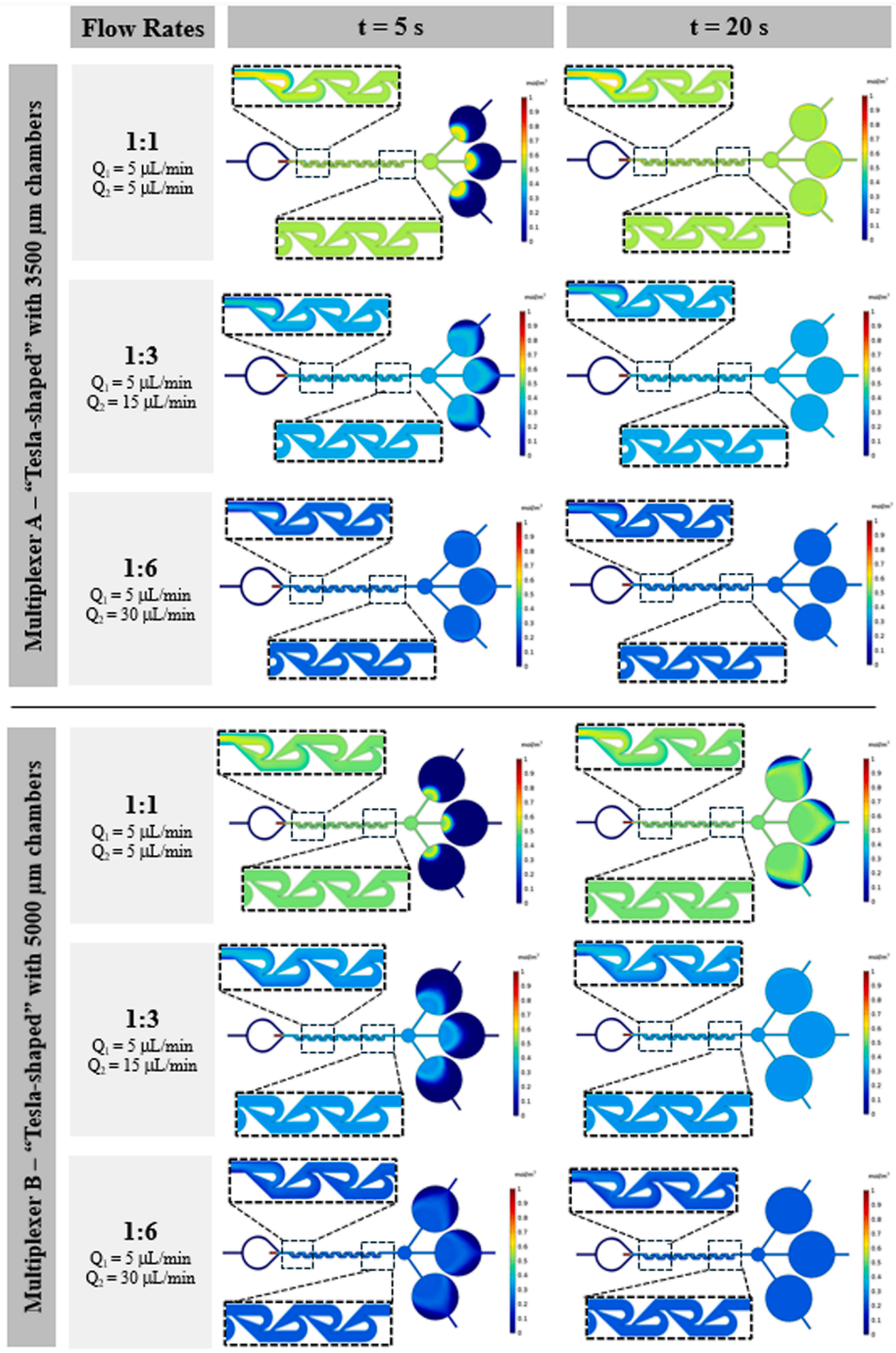


Fig. 6. Concentration of the solute species (mol/m^3) after 5 s and 20 s along the "Tesla-shaped" multiplexers, for both 3500 µm and 5000 µm chamber diameters, at different flow ratios: 1:1 ($Q_1 = 5$ µL/min and $Q_2 = 5$ µL/min); 1:3 ($Q_1 = 5$ µL/min and $Q_2 = 15$ µL/min) and 1:6 ($Q_1 = 5$ µL/min and $Q_2 = 30$ µL/min).

3.1. Governing equations

The laminar flow is governed by the Navier-Stokes equations, which express the motion of a fluid. Momentum conservation is described by the following differential Equation 3 [51]:

$$\rho\left(\underbrace{\frac{\partial \boldsymbol{u}}{\partial t}+\boldsymbol{u}\cdot\nabla\boldsymbol{u}}_{1}\right)=\underbrace{-\nabla p}_{2}+\underbrace{\nabla\cdot\left(\mu\left(\nabla\boldsymbol{u}+(\nabla\boldsymbol{u})^{T}\right)-\frac{2}{3}\mu(\nabla\cdot\boldsymbol{u})\boldsymbol{I}\right)}_{3}+\underbrace{\boldsymbol{F}}_{4} \quad (3)$$

where $\boldsymbol{u}$ is the velocity vector (m/s), p the pressure (Pa), $\boldsymbol{F}$ the external forces applied (N/m^3), T the transpose of the matrix and $\boldsymbol{I}$ the identity matrix. Additionally, term 1 represents the inertial forces, term 2 the pressure forces, term 3 the viscous forces and term 4 the external forces applied to the fluid. In the case of incompressible flows, the $-\frac{2}{3}\mu(\nabla\cdot\boldsymbol{u})$I part of term 3 can be removed from the viscous forces term [52]. The Navier-Stokes law also considers the continuity equation, reflecting the conservation of mass, as in Equation 4 [53]:

$$\nabla\cdot\boldsymbol{u}=0 \quad (4)$$

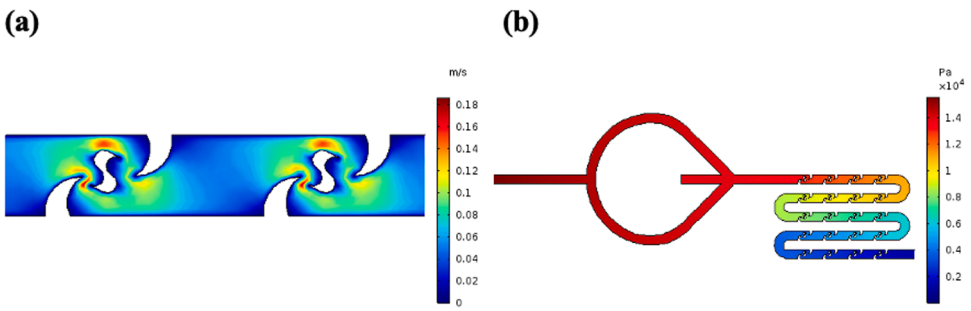


Fig. 7. Steady-state distribution of (a) velocity magnitude (m/s) and (b) pressure (Pa) in the mixing region of the "half-moon-shaped" multiplexer.

The governing equation of the transport of diluted species is described in Equation 5 [54]:

$$\frac{\partial c}{\partial t} + \boldsymbol{u}\cdot\nabla c = \nabla\cdot(D\nabla c) + R \tag{5}$$

where c represents the concentration of the species (mol/m^3), D (m^2/s) the characteristic diffusion coefficient of the species and R the species reaction rate (mol/(m^3·s)).

3.2. Domain and boundary conditions

The domain and boundary conditions considered in the numerical model are detailed below, for the laminar flow and transport of diluted species, respectively:

Laminar flow: Water, with incompressible condition, was established as the working fluid, with constant dynamic viscosity of 1.00394 mPa·s and 999.615 kg/m^3 density, at room temperature (293.15 K). To ensure the impermeability of the channel walls, a non-slip condition was defined, imposing zero velocity at all boundaries and confining the flow strictly to the microchannels. The pressure at the outlet was set to 0 Pa, allowing for a natural outflow. Regarding the inlets, different flow rate ratios between them (1:1, 1:3, and 1:6) were investigated to assess their influence on the mixing performance. The inlet Q_1 was set at 5 μL/min as reference flow while varying the inlet Q_2 from 5 to 30 μL/min. Therefore, the following initial flow rate ratios were studied: 1:1 ($Q_1 = 5$ μL/min and $Q_2 = 5$ μL/min); 1:3 ($Q_1 = 5$ μL/min and $Q_2 = 15$ μL/min) and 1:6 ($Q_1 = 5$ μL/min and $Q_2 = 30$ μL/min).

Transport of diluted species: The transport of the species resulted from the velocity field obtained by solving the laminar flow equations and the species diffusion properties. The initial species concentration was defined as 1 mol/m^3 at inlet 1 (with a fixed flow rate of 5 μL/min) and 0 mol/m^3 at inlet 2 (with variable flow rates, as previously detailed). The walls were defined with a "no flux" conditions, assuring that the species only flow in the microchannel. The model assumed a solute diffusion coefficient of 1×10^{-9} m^2/s.

3.3. Domain, mesh and solver

A preliminary 3D simulation study was first conducted to evaluate the adequacy of a 2D model as representative of the 3D model (see Supplementary Material, Figure S. 1-4). Given the close agreement between the 2D and 3D results, 2D transient simulations were subsequently employed for all geometries, which require lower computational cost. Additionally, a mesh independence study was also performed to assess the influence of the selected mesh resolution on the accuracy of the numerical results. For this purpose, the maximum velocity was computed for each geometry at a flow ratio of 1:1 using the different default mesh refinement levels available in the software, and the results are presented in Table 1 and Fig. 3.

Based on the results, a default coarse refinement mesh was considered for all geometries, providing an adequate balance between numerical accuracy and computational cost. The different meshes, detailed in Fig. 4, were composed of unstructured meshes, combining both triangular and quadrilateral elements, resulting in a total of 11703 elements for the multiplexer A, 9969 elements for the multiplexer B, 19589 elements for the multiplexer C and 15739 elements for the multiplexer D (see Figs. 1 and 2). All meshes assured a good accuracy of results, with average quality of the elements >70% (0.762 for multiplexer A, 0.750 for multiplexer B, 0.749 for multiplexer C and 0.731 for multiplexer D). The numerical simulations were performed using the time-dependent PARDISO (Parallel Direct Solver) algorithm, for a total duration of 20 s and a time step of 0.2 s.

3.4. Numerical results

This section presents and discusses the numerical results obtained for the different studied multiplexer platforms.

3.4.1. "Tesla-shaped" multiplexer

Fig. 5 (a) shows the distribution of the steady-state velocity magnitude through the mixing structure of the "Tesla-shaped" micromixer. It can be observed that the regions of highest velocity correspond to the sections where the channel narrows, since the available cross-sectional area for the flow decreases significantly. At the curvatures and corners of the channel, the velocity also increases, as the flow is forced to change direction. In Fig. 5 (b), the steady-state pressure field along the mixing region is shown, with a progressive decrease in pressure from the inlets to the outlet, reflecting the intended flow behavior.

The distribution of the concentration of the solute species through the "Tesla-shaped" multiplexer, at 5 s and 20 s, can be observed in Fig. 6. Overall, by qualitative observation of the solute concentrations (by the color scale), both configurations of the "Tesla-shaped" microchannel, with different reaction chamber diameters, demonstrated excellent performance in terms of mixing efficiency and fluid transport to the different chambers, for all the considered flow rate ratios (supported by Supplementary Material, Figure S. 5 (a) and (b)). The simulations indicate that mixing is nearly complete by the second mixing structure, and at higher flow ratios, the inlet with higher concentration predominates, which is reflected in the mixture at the end of the mixing region. It is also observed that, for the two highest flow ratios, the chambers are uniformly loaded, reaching near-complete volumes after 20 s in both diameters. These results demonstrate the "Tesla-shaped" multiplexer's capability to achieve rapid and uniform fluid distribution under the tested conditions.

3.4.2. "Half-moon-shaped" multiplexer

According to Fig. 7 (a), which illustrates the distribution of the steady-state velocity magnitude in the mixing structure of "half-moon-shaped" micromixer, higher velocities are observed, as expected, in the channel constrictions caused by the central obstacles. Velocity also increases at the vertices of the semicircular half-moon structures due to the change they cause in flow direction, while at the vertices of these structures adjacent to the upper and lower channel walls, the velocity approaches zero, potentially leading to particle accumulation zones.

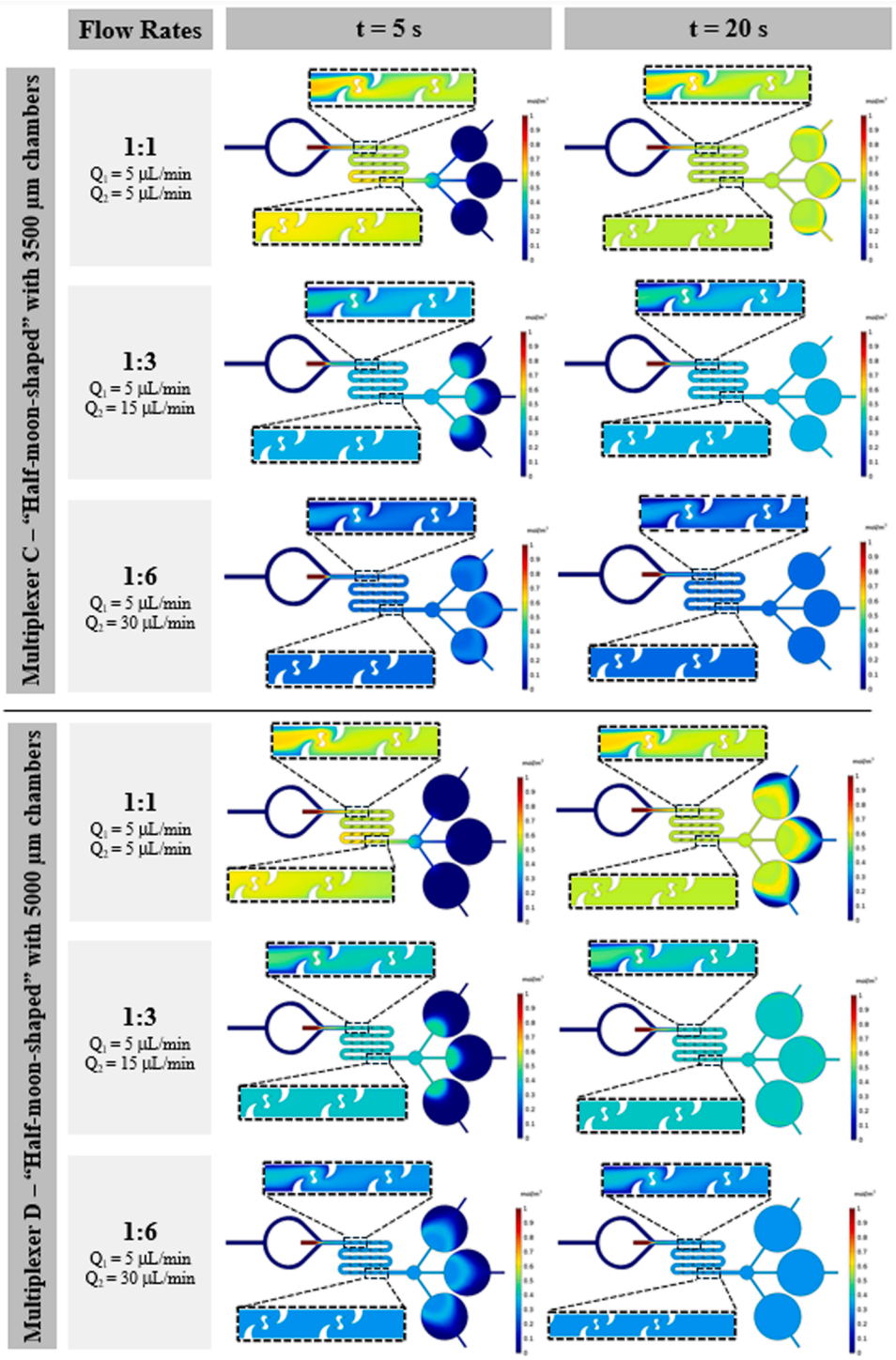


Fig. 8. Concentration of the solute species (mol/m^3) after 5 s and 20 s along the "half-moon-shaped" multiplexers, for both 3500 µm and 5000 µm chamber diameters, at different flow ratios: 1:1 ($Q_1 = 5$ µL/min and $Q_2 = 5$ µL/min); 1:3 ($Q_1 = 5$ µL/min and $Q_2 = 15$ µL/min) and 1:6 ($Q_1 = 5$ µL/min and $Q_2 = 30$ µL/min).

Regarding the steady-state pressure distribution, presented in Fig. 7 (b), a clear pressure gradient is visible from the inlets to the outlet, driving the mixing flow along the microchannel.

Fig. 8 shows the distribution of the concentration of the solute species in the "half-moon-shaped" multiplexer, at 5 s and 20 s. Similarly to the previous geometry, both designs, with different chamber diameters, and for all flow rate ratios, exhibited good mixing and fluid driving to the chambers (supported by Supplementary Material, Figure S. 5 (c) and (d)). The numerical results show that mixing is almost complete by the end of the first serpentine segment, and the chambers are practically filled after 20 s at the two highest flow ratios. Thus, this multiplexer geometry can be also considered, from the obtained numerical results, as a viable alternative for achieving efficient mixing and fluid transport to the chambers for the studied flow rates.

3.4.3. *Numerical evaluation of mixing efficiency*

In addition to the concentration profile analysis, the numerical mixing performance was quantitatively assessed for both micromixer geometries under all flow ratios over a 20 s simulation. A cross-sectional line extending across the channel width and positioned at the end of the

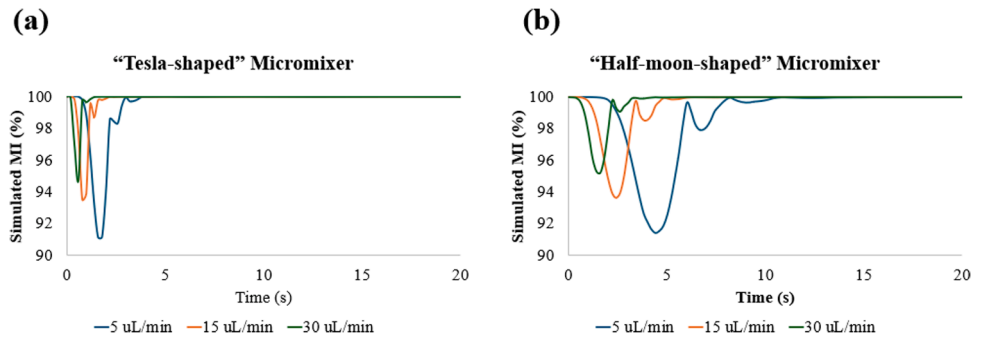


Fig. 9. Simulated mixing efficiency index (%) over 20 s for the studied micromixer geometries under the different inlet flow rate ratios: 1:1 ($Q_1 = 5$ μL/min, $Q_2 = 5$ μL/min), 1:3 ($Q_1 = 5$ μL/min, $Q_2 = 15$ μL/min), and 1:6 ($Q_1 = 5$ μL/min, $Q_2 = 30$ μL/min). (a) "Tesla-shaped" micromixer and (b) "half-moon-shaped" micromixer.

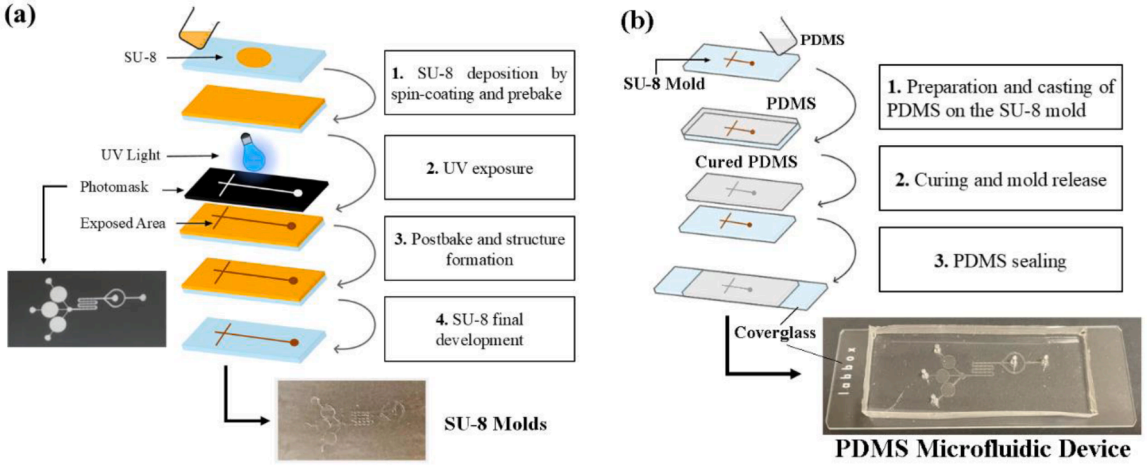


Fig. 10. Schematic fabrication process of a representative multiplexer microfluidic device, divided into two phases: (a) SU-8 molds fabricated by UV photolithography and (b) replica molding of PDMS and microfluidic device.

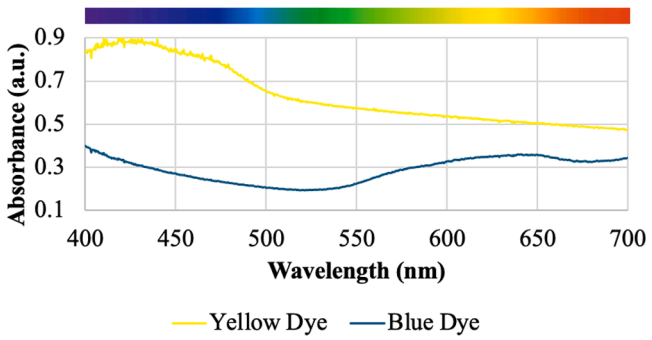


Fig. 11. Absorbance spectra of the yellow and blue test fluids before entering the inlets.

mixing section, was defined to obtain the concentration profile along the channel. The indices were calculated from Eqs. 6, 7 and 8, described by Waqas et al. [55]:

$$MI_{sim} = \left(1 - \sqrt{\frac{\sigma^2}{\sigma_{max}^2}}\right) \times 100 \quad (6)$$

$$\sigma = \sqrt{\frac{1}{n}\sum_{i=1}^{n}(c_i - \overline{c})} \quad (7)$$

$$\sigma_{max} = \sqrt{\overline{c}(1-\overline{c})} \quad (8)$$

where MI_{sim} is the simulated mixing efficiency index (%), σ the standard deviation of the concentration distribution along the cross-sectional line, σ_{max} the maximum standard deviation associated with the corresponding mean concentration $\overline{c}$ and c_i the concentration at each data point (i) of the line. The resulting simulated indices are presented in Fig. 9 (a) and (b). After an initial decrease caused by the introduction of the inlet streams, stable mixing index values of almost 100% were achieved within 20 s, indicating homogeneous concentration mixing for both geometries.

4. Experimental analysis

4.1. Multiplexer fabrication

The multiplexers, following the methodology reported by Pinto et al. [56], were fabricated in polydimethylsiloxane (PDMS) by replica molding, using SU-8 25 epoxy molds fabricated by ultraviolet (UV)-soft lithography, in a rapid and inexpensive method that does not require cleanroom facilities. PDMS, a cost-effective elastomer, was selected due to its biocompatibility, low-cost, and optical transparency, particularly advantageous for microsystems employing optical detection. Initially, the CAD-designed geometries were printed onto transparent photographic sheets and used as photomasks. The overall fabrication process, described in Fig. 10, can then be divided into two main stages. In the first one, Fig. 10 (a), the SU-8 molds were fabricated via UV-photolithography, enabling 25 μm-thick structures using the photomasks printed previously. In the second stage, Fig. 10 (b), PDMS replica molding was performed by preparing a 10:1 ratio of pre-polymer base/cure agent mixture, poured into the molds and cured at 80°C during 45 min. After curing, the PDMS structures were detached, access

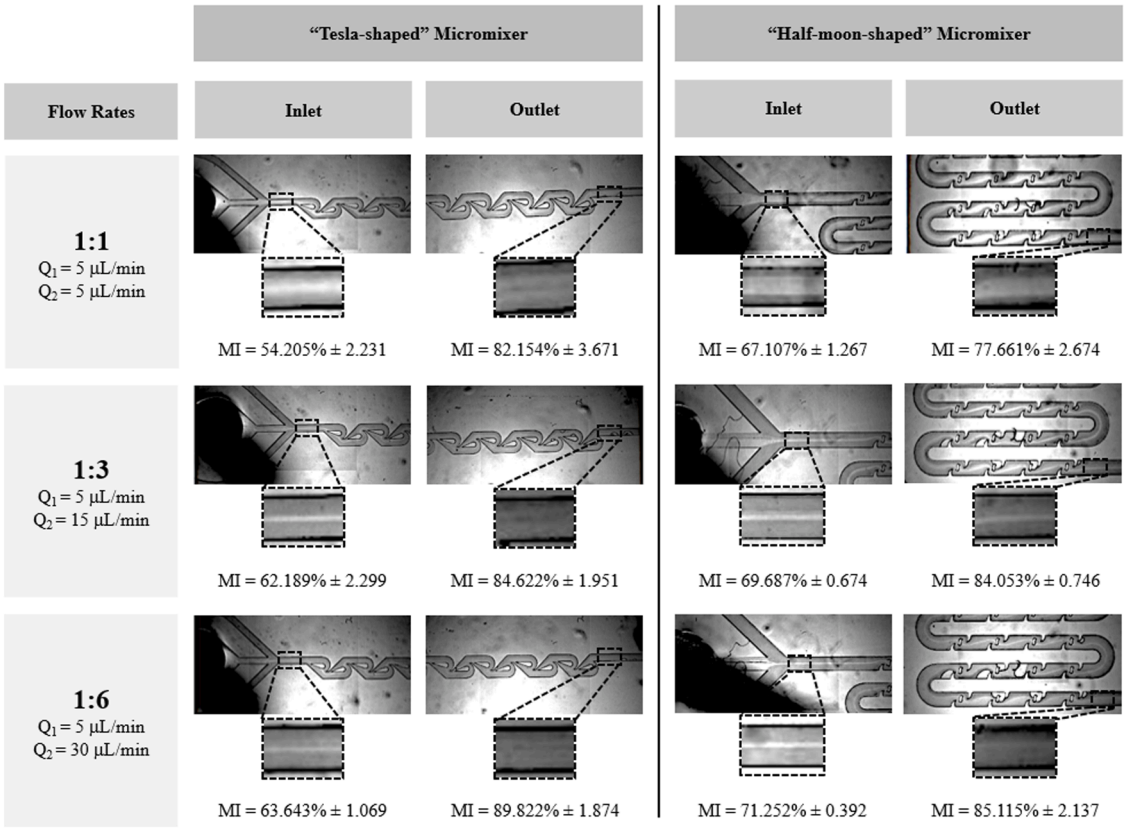


Fig. 12. Optical microscopy images (10 × magnification) and corresponding mixing efficiency index (MI, %) at the inlet and outlet regions of the "Tesla-shaped" and "half-moon-shaped" micromixers for different flow rate ratios: 1:1 ($Q_1 = 5$ μL/min, $Q_2 = 5$ μL/min), 1:3 ($Q_1 = 5$ μL/min, $Q_2 = 15$ μL/min), and 1:6 ($Q_1 = 5$ μL/min, $Q_2 = 30$ μL/min). The yellow fluid corresponds to the fluid entering the central inlet (lighter fluid), and the blue fluid corresponds to the fluid entering the lateral inlet (darker fluid).

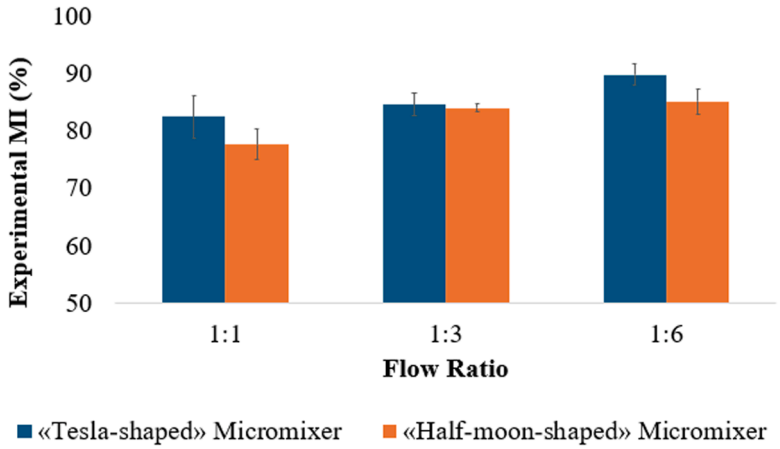


Fig. 13. Experimental mixing efficiency index (%) calculated at the outlet of each micromixer geometries studied, for the different flow rate ratios between the two inlets: 1:1 ($Q_1 = 5$ μL/min, $Q_2 = 5$ μL/min), 1:3 ($Q_1 = 5$ μL/min, $Q_2 = 15$ μL/min), and 1:6 ($Q_1 = 5$ μL/min, $Q_2 = 30$ μL/min).

holes were opened with a metal tip pen to form inlets and outlets and finally the devices were bonded to glass substrates using an oxygen plasma treatment (Plasma system type Zepto model 5, Dienner Electronic GmbH, Ebhausen, Germany).

4.2. Experimental setup

The setup for the experimental analysis of the multiplexer microfluidic platforms comprises four systems: microfluidic system, syringe pumping system, microscopy imaging and spectrophotometry setup. The microfluidic system included the PDMS microchannels and polytetrafluoroethylene (PTFE) passive bubble extractors (Elveflow, Paris, France) attached to the inlets, to prevent bubbles formation inside the microchannels. The pump system consisted of a two-syringe pump platform (neMESYS Syringe Pump, Cetoni, Korbussen, Germany) for precise control and manipulation of the fluid flows and 0.8 mm PTFE tubes. For imaging, the microscopy system comprised an inverted optical microscope (IX71, Olympus, Tokyo, Japan), combined with a monochromatic high-speed camera (Photron Fastcam SA3, Motion Engineering Company, Westfield, USA). Finally, the spectrophotometry system, used to assess the colorimetric profile of the mixtures at each outlet/chamber, consisted of a 200 W tungsten light source (NRC-

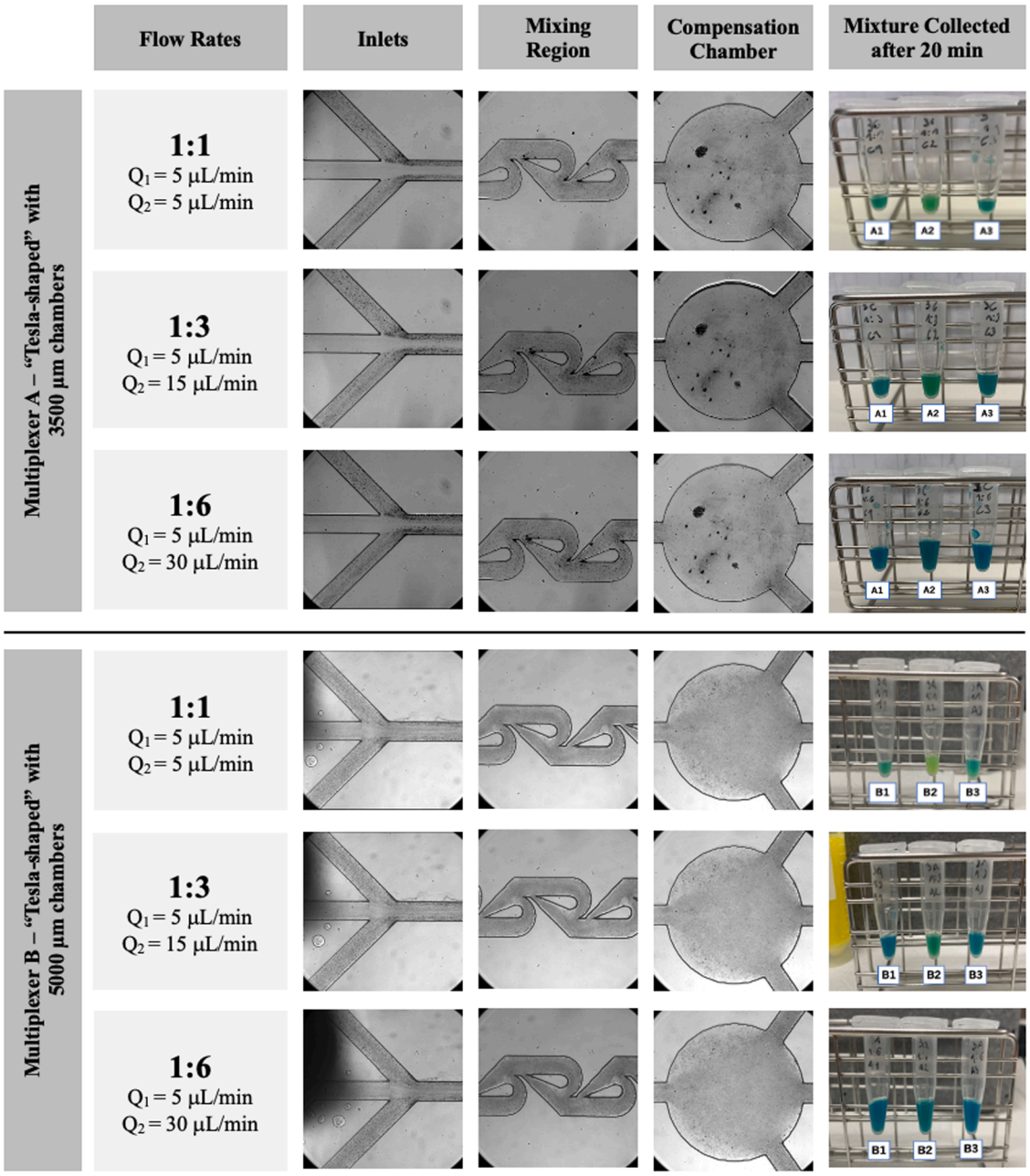


Fig. 14. Optical microscopy images (15 × magnification) of the "Tesla-shaped" multiplexers and volumes of collected mixture at the outlet of the microchannel, after 20 minutes, at different flow rate ratios: 1:1 ($Q_1 = 5$ µL/min, $Q_2 = 5$ µL/min), 1:3 ($Q_1 = 5$ µL/min, $Q_2 = 15$ µL/min), and 1:6 ($Q_1 = 5$ µL/min, $Q_2 = 30$ µL/min). The yellow fluid corresponds to the fluid entering the central inlet, and the blue fluid corresponds to the fluid entering the lateral inlet.

6334NS, Newport, Irvine, USA) directed into a darkened sample holder to prevent external light interference, which was in turn connected to a spectrophotometer with an integrated detector and monochromator (AvaSpec-ULS2048XL EVO, Avantes, Apeldoorn, Netherlands).

The multiplexers were evaluated using 1 g of blue and yellow dyes diluted in 1 mL of deionized water (these colors were selected for better visualization of the flowing species) and the devices were subjected to continuous flow tests for 20 minutes under the different studied flow ratios. The fluids outputted from the three outlets were collected into Eppendorf tubes, and their volumes were quantified using micropipettes. Next, for colorimetric analysis of the output samples, 35 µL of each mixture fluid was diluted into 1 mL of deionized water to ensure consistent measurement conditions, and the diluted samples were measured using the spectrophotometric setup, in 1 cm pathlength cuvettes, with the absorbance spectra recorded between 400 and 700 nm.

Fig. 11 presents the absorbance spectra of the yellow and blue test fluids, inserted at the microchannel inlets. The yellow inlet exhibited a predominant absorbance between 400 and 470 nm (violet/blue region), while the blue solution showed a peak in the violet region and a higher absorbance around 650 nm (orange region). As a result, the spectra obtained for the fluids collected at the outlets of the microchannels with the different geometries is expected to display higher absorbance in the violet and orange regions, depending on the mixing ratios. To quantitatively assess these spectral variations, the absorbance values at 400 nm (violet) and 640 nm (orange), as well as the ratio between the two values ($A_{400\ nm}$ / $A_{640\ nm}$), were registered at each outlet for the different multiplexers and flow ratios. All experiments were performed in three runs to ensure reproducibility (n=3).

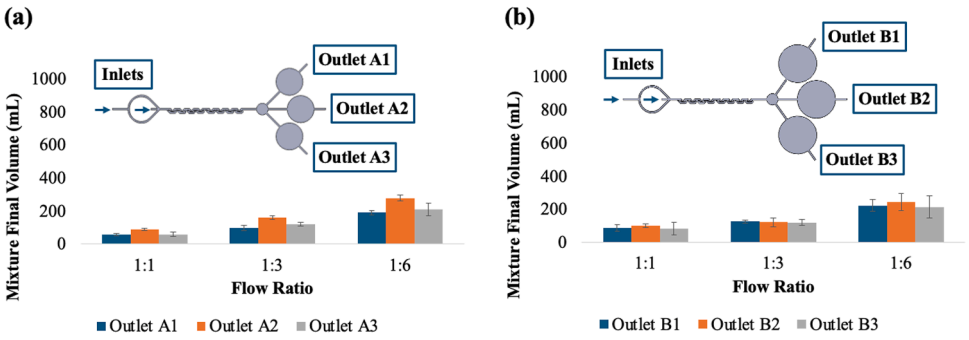


Fig. 15. Mean and standard deviation (n = 3) of the volumes (μL) of mixture collected after 20 minutes at each outlet of the "Tesla-shaped" multiplexers: (a) 3500 μm reaction chambers and (b) 5000 μm chambers, at flow rate ratios of 1:1 ($Q_1 = 5$ μL/min, $Q_2 = 5$ μL/min), 1:3 ($Q_1 = 5$ μL/min, $Q_2 = 15$ μL/min), and 1:6 ($Q_1 = 5$ μL/min, $Q_2 = 30$ μL/min).

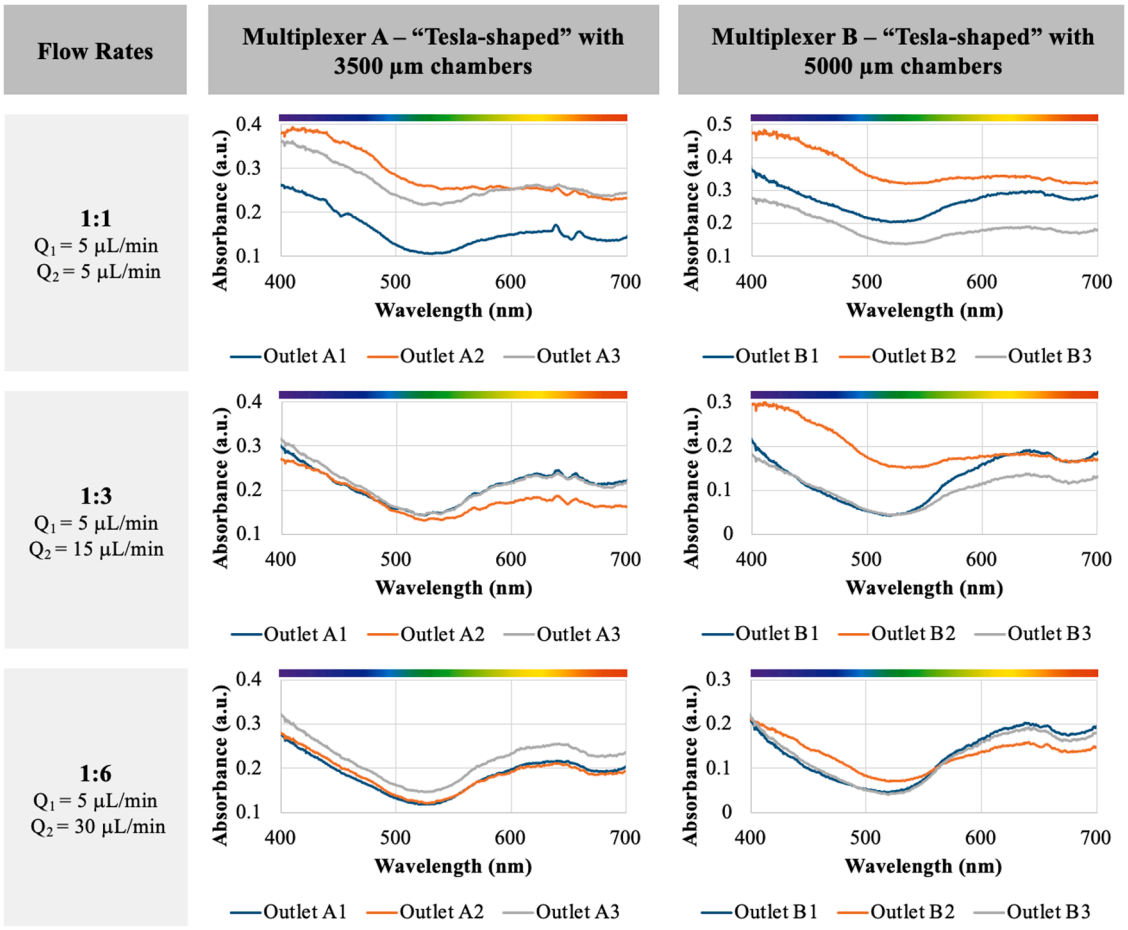


Fig. 16. Absorbance spectra (a.u.) of the mixtures collected after 20 minutes at each outlet of the "Tesla-shaped" multiplexers, at flow rate ratios: 1:1 ($Q_1 = 5$ μL/min, $Q_2 = 5$ μL/min), 1:3 ($Q_1 = 5$ μL/min, $Q_2 = 15$ μL/min), and 1:6 ($Q_1 = 5$ μL/min, $Q_2 = 30$ μL/min).

4.3. Experimental results

This section presents the experimental results of the multiplexers' flows, covering both the mixing efficiency analysis and the outlet fluid characterization, obtained from each reaction chamber and for the different flow rate ratios.

4.3.1. Experimental assessment of mixing performance

A preliminary evaluation of the mixing efficiency in the multiplexers' mixing region (without considering the post-mixing region chambers) was conducted prior to their full characterization, based on microscopy image analysis and calculus of the mixing index for each flow ratios. To calculate the mixing indices, the black and white images obtained by microscopy were processed in imageJ software, and Eq. 9 was applied, as reported by Fu et al. [57]:

$$MI_{exp} = \left(1 - \frac{1}{\bar{I}}\sqrt{\frac{\sum_{i=1}^{N}(I(i) - \bar{I})^2}{N}}\right) \times 100 \quad (9)$$

where MI_{exp} is the experimental mixing efficiency index (%), $\bar{I}$ the average intensity of the region of interest (ROI) corresponding to the channel inlet and outlet regions, $I_{(i)}$ the intensity of pixel i and N the total

Table 2
Absorbance (a.u.) feature characterization of each outlet under the different flow ratios for "Tesla-shaped" multiplexers, including mean absorbance standard deviation (SD), absorbance values at 400 nm and 640 nm, and the corresponding 400/640 nm absorbance ratio. The mean absorbance SD corresponds to the average of all standard deviation values calculated for each wavelength (n=3).

		Multiplexer A – "Tesla-shaped" with 3500 μm chambers			Multiplexer B – "Tesla-shaped" with 5000 μm chambers		
		Outlet A1	Outlet A2	Outlet A3	Outlet B1	Outlet B2	Outlet B3
1:1	**Mean Absorbance SD**	0.123	0.006	0.009	0.001	0.001	0.009
$Q_1 = 5$ μL/min	$A_{400\ nm}$	0.263	0.381	0.363	0.361	0.475	0.277
$Q_2 = 5$ μL/min	$A_{640\ nm}$	0.169	0.255	0.262	0.296	0.343	0.189
	$A_{400\ nm}$ / $A_{640\ nm}$ **Ratio**	1.555	1.494	1.384	1.221	1.386	1.465
1:3	**Mean Absorbance SD**	0.023	0.012	0.002	0.005	0.010	0.003
$Q_1 = 5$ μL/min	$A_{400\ nm}$	0.298	0.270	0.314	0.212	0.295	0.181
$Q_2 = 15$ μL/min	$A_{640\ nm}$	0.244	0.187	0.238	0.188	0.181	0.136
	$A_{400\ nm}$ / $A_{640\ nm}$ **Ratio**	1.219	1.448	1.320	1.123	1.631	1.331
1:6	**Mean Absorbance SD**	0.006	0.001	0.007	0.022	0.013	0.127
$Q_1 = 5$ μL/min	$A_{400\ nm}$	0.275	0.279	0.320	0.209	0.212	0.217
$Q_2 = 30$ μL/min	$A_{640\ nm}$	0.216	0.210	0.254	0.201	0.158	0.190
	$A_{400\ nm}$ / $A_{640\ nm}$ **Ratio**	1.275	1.333	1.262	1.039	1.344	1.142

number of pixels. This calculation is based on the variation in grayscale of pixel intensity within the selected ROI of the mixing section and quantified by the standard deviation of the pixel intensities. For instance, in a region located near the inlets, the distinction between the two dye solutions is clearly observable (darker lateral regions corresponding to the blue dye and a lighter central region corresponding to the yellow), resulting in higher pixel intensity variations, as the species have not yet undergone significant mixing, as observed in Fig. 12. In contrast, at the end of the mixing section, the solution becomes more uniformly distributed throughout the channel, leading to a more homogeneous grayscale intensity distribution and consequently lower intensity variations (minor standard deviation between the pixel intensities in the ROI). This behavior is indicative of effective mixing and is reflected by the higher mixing index values observed downstream. Figs. 12 and 13 present microscopy images and the calculated mixing indices, respectively, for both micromixers, for the different flow rate ratios.

Overall, the "Tesla-shaped" micromixer exhibited better mixing efficiency than the "half-moon-shaped" one, with a more uniform distribution at the end of the channel, in agreement with slightly higher mixing index values. In the "half-moon-shaped" micromixer, it is still visible a slight color variation at the end of the microchannel, indicating that complete mixing was not achieved. The minor differences in the "half-moon-shaped" geometry may be attributed to air-bubble accumulation in regions adjacent to the vertices, that can influence the mixing performance. Moreover, the mixture homogenization improves at higher flow rates, as enhanced inertial effects promote chaotic advection and increase the interfacial contact between the fluid streams. In summary, these results indicate that both micromixer geometries are highly effective in achieving uniform mixing across the channels under the tested conditions.

4.3.2. Characterization of the multiplexer outlets

The following sub-sections describe the experimental results of the multiplexers' outlet evaluation, by analyzing the microscope images, the mixtures obtained at each outlet for the different flow ratios, and the corresponding quantified volumes and absorbance spectra.

4.3.2.1. "Tesla-shaped" multiplexer. Fig. 14 presents optical microscopy images and the fluid volumes collected from each outlet of "Tesla-shaped" multiplexers. By observing the images, highly efficient mixing was achieved for all chamber diameters and across all the considered flow rate ratios (in agreement with the numerical simulations). In contrast, based on the analysis of the collected volumes and their corresponding color intensities, all multiplexers exhibited slight color discrepancies between the central outlets (A2 and B2 – more green-toned) and the lateral ones (with a more pronounced blue coloration). This phenomenon can be attributed to the laminar flow profile, which tends to produce more pronounced mixing in the center of the stream, where the velocity is higher. It is even more noticeable in the multiplexer with 5000 μm diameter chambers, where the disproportion between the compensation and main chamber diameters is more evident, resulting in insufficiently stabilized mixing in the compensation chamber located previously to the detection chambers.

The sample volumes collected from each outlet after 20 minutes of continuous flow are represented in Fig. 15 and Table S. 1-2 in Supplementary Material. Beyond the expected increase in collected volume with higher flow rate ratios, minor variations were observed in the central outlets (A2 and B2) compared to the lateral outlets, an issue that could be further mitigated by increasing the width of the channel connecting the compensation and reaction chambers, thereby reducing the fluid velocity. It was observed, for the 3500 μm chamber, CV around or below 25%, while, for the 5000 μm chamber, these values were substantially lower, below or around 10%, demonstrating that increasing the reaction chamber diameter contributes to a better volume distribution of the sample. However, these differences were not statistically significant ($p > 0.05$), indicating good performance of these geometries in terms of fluid transport (Supplementary Material, Table S. 5).

As illustrated in Fig. 16, all spectra exhibit the two prominent absorbance regions as previously stated (in section 4.2). It is observed that, with increasing flow rate ratios, the absorbance in the orange region becomes more pronounced compared to the violet region, resulting in a higher proportion of the complementary blue coloration at the outlets. These observations were corroborated by the quantitative results reported in Table 2, where the absorbance ratios ($A_{400\ nm}$ / $A_{640\ nm}$) became progressively lower with increasing flow ratios, due to the more pronounced 640 nm absorbance peak. Overall, the similar spectral patterns observed and equivalent $A_{400\ nm}$ / $A_{640\ nm}$ ratios across all outlets, under the different flow rate ratios, have demonstrated once again the efficiency of mixing and fluid distribution in these multiplexers. In particular, the geometry with 3500 μm chambers exhibited more consistent $A_{400\ nm}$ / $A_{640\ nm}$ values between the outlets. However, some exceptions were noted: in the lateral chamber outlet A1 at a 1:1 flow ratio, the spectrum displayed lower absolute absorbance values compared to the other outlets (A2 and A3), indicating a less colored intense solution; in the multiplexer with 5000 μm diameter chambers at a 1:1 ratio, discrepancies in absorbance values were observed; and, finally, slightly higher $A_{400\ nm}$ / $A_{640\ nm}$ ratios were registered at the central outlet (A2 and B2) than at the lateral outlets for each flow ratio (except at a 1:1 ratio), indicating a higher proportion of yellow and consequently, a greener coloration of the collected samples at the central outlets.

4.3.2.2. "Half-moon-shaped" multiplexer. The microscopy images of the "half-moon-shaped" multiplexers are presented in Fig. 17, showing satisfactory mixing along the microchannel, similar to what was observed in the "Tesla-shaped" geometry and consistent with the numerical simulation results. However, as evidenced by the mixture volumes collected at the chamber outlets, and validated by the mixing indices calculated in section 4.3.1, mixing was less uniform in these multiplexers across all flow rate ratios. Here, the mixture in the central chambers appeared with more pronounced green coloration than in the lateral ones, particularly in the multiplexer with 5000 μm diameter chambers. This fact can be attributed not only to the less effective stabilization of the mixture in the compensation chamber, as observed previously, but also to the overall lower mixing efficiency of the mixing section.

As observed in Fig. 18 and Table S. 3-4 in Supplementary Material, the outlet sample volumes collected and quantified after 20 minutes of flow, presented more irregular values compared to those collected from the "Tesla-shaped" multiplexers. In the geometry with 3500 μm diameter chambers, CV around or below 25% were observed and significant differences between the lateral outlets (C1 and C3) and the central one (C2) were identified through the statistical analysis (Supplementary Material, Table S.5) ($p < 0.05$). Conversely, in the multiplexer with 5000

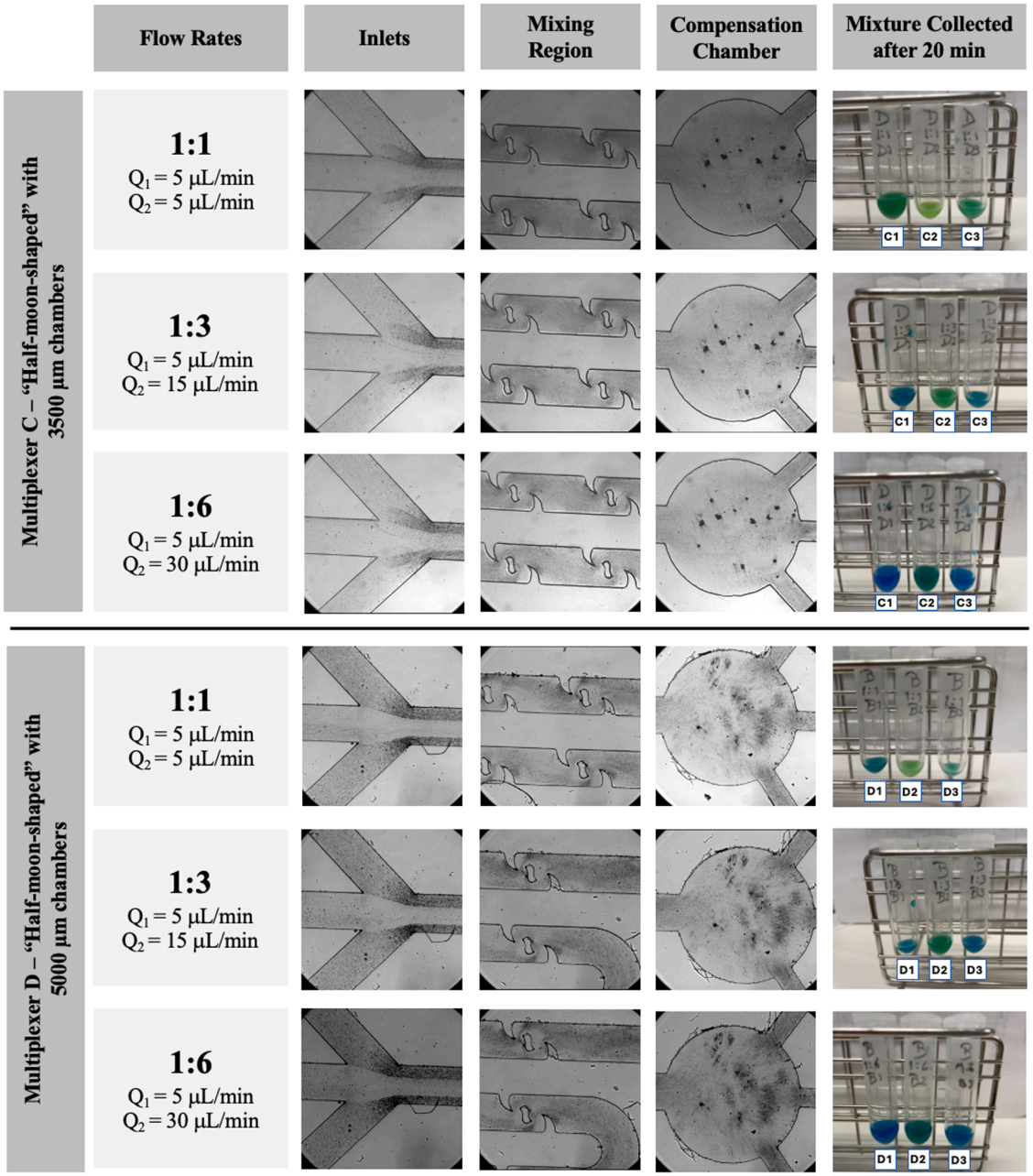


Fig. 17. Optical microscopy images (15 × magnification) of the "half-moon-shaped" multiplexers and volumes of collected mixture at the outlet of the microchannel, after 20 minutes, at different flow rate ratios: 1:1 ($Q_1 = 5$ μL/min, $Q_2 = 5$ μL/min), 1:3 ($Q_1 = 5$ μL/min, $Q_2 = 15$ μL/min), and 1:6 ($Q_1 = 5$ μL/min, $Q_2 = 30$ μL/min). The yellow fluid corresponds to the fluid entering the central inlet, and the blue fluid corresponds to the fluid entering the lateral inlet.

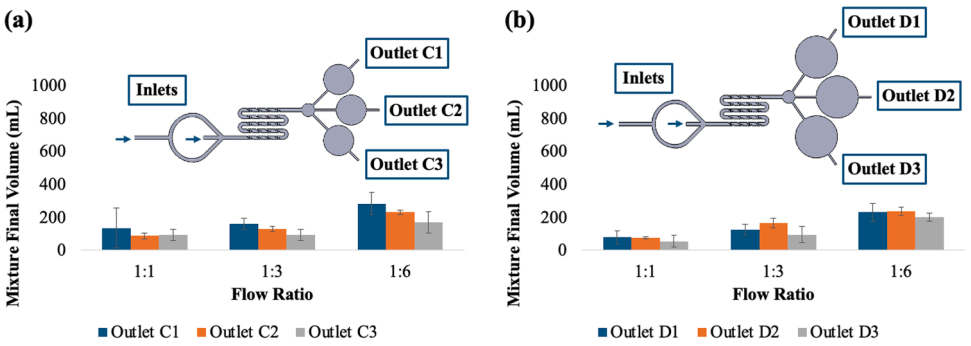


Fig. 18. Mean and standard deviation (n = 3) of the volumes (μL) of mixture collected after 20 minutes at each outlet of the "half-moon-shaped" multiplexers: (a) 3500 μm reaction chambers and (b) 5000 μm chambers, at flow rate ratios of 1:1 (Q_1 = 5 μL/min, Q_2 = 5 μL/min), 1:3 (Q_1 = 5 μL/min, Q_2 = 15 μL/min), and 1:6 (Q_1 = 5 μL/min, Q_2 = 30 μL/min).

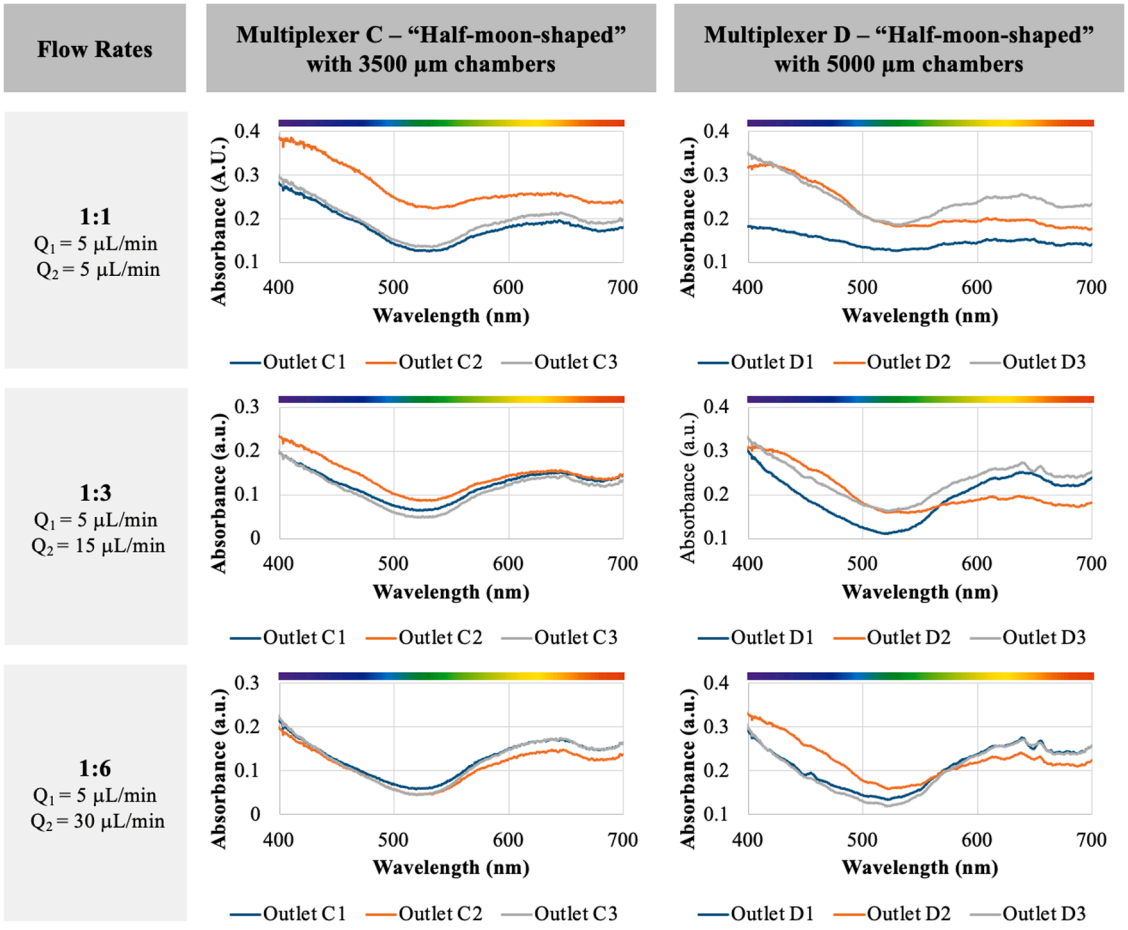


Fig. 19. Absorbance spectra (a.u.) of the mixtures collected after 20 minutes at each outlet of the "half-moon-shaped" multiplexers at flow rate ratios: 1:1 (Q_1 = 5 μL/min, Q_2 = 5 μL/min), 1:3 (Q_1 = 5 μL/min, Q_2 = 15 μL/min), and 1:6 (Q_1 = 5 μL/min, Q_2 = 30 μL/min).

μm diameter chambers, the collected volumes were more uniformly distributed among the outlets, with lower CV values, and statistically supported ($p > 0.05$), demonstrating once again that volume distribution improved with increasing chamber diameter.

The absorbance spectra of the solutions collected from the outlets of the "half-moon-shaped" multiplexers are presented in Fig. 19. As stated on the previous multiplexers, the central outlets here also exhibited a stronger green component across all flow ratios in both geometries, as confirmed by higher $A_{400\ nm}$ / $A_{640\ nm}$ ratio values listed in Table 3.

Apart from this aspect, the geometry with 3500 μm diameter chambers showed better results regarding mixing efficiency for all ratios, with similar spectral profiles and consistent absorbance peaks at 400 and 640 nm between outlets, in contrast with the geometry with 5000 μm chambers. In this case, distinct spectra across outlets were observed, along with substantial differences in the $A_{400\ nm}$ / $A_{640\ nm}$ ratios observed at the central outlet (D2) compared with the lateral outlets (D1 and D3), particularly for the 1:1 and 1:3 flow ratios.

Table 3
Absorbance (a.u.) feature characterization of each outlet under the different flow ratios for "half-moon-shaped" multiplexers, including mean absorbance standard deviation (SD), absorbance values at 400 nm and 640 nm, and the corresponding 400/640 nm absorbance ratio. The mean absorbance SD corresponds to the average of all standard deviation values calculated for each wavelength (n=3).

		Multiplexer C – "Half-moon-shaped" with 3500 μm chambers			Multiplexer D – "Half-moon-shaped" with 5000 μm chambers		
		Outlet C1	Outlet C2	Outlet C3	Outlet D1	Outlet D2	Outlet D3
1:1	**Mean Absorbance SD**	0.012	0.001	0.014	0.012	0.010	0.018
$Q_1 = 5$ μL/min	$A_{400\ nm}$	0.280	0.385	0.296	0.184	0.320	0.349
$Q_2 = 5$ μL/min	$A_{640\ nm}$	0.195	0.257	0.211	0.153	0.198	0.255
	$A_{400\ nm}$ / $A_{640\ nm}$ **Ratio**	1.434	1.499	1.407	1.200	1.617	1.368
1:3	**Mean Absorbance SD**	0.008	0.024	0.000	0.007	0.016	0.043
$Q_1 = 5$ μL/min	$A_{400\ nm}$	0.198	0.233	0.198	0.299	0.309	0.329
$Q_2 = 15$ μL/min	$A_{640\ nm}$	0.150	0.155	0.140	0.251	0.195	0.273
	$A_{400\ nm}$ / $A_{640\ nm}$ **Ratio**	1.322	1.508	1.415	1.193	1.584	1.204
1:6	**Mean Absorbance SD**	0.001	0.002	0.001	0.037	0.006	0.070
$Q_1 = 5$ μL/min	$A_{400\ nm}$	0.215	0.197	0.221	0.292	0.329	0.298
$Q_2 = 30$ μL/min	$A_{640\ nm}$	0.171	0.145	0.170	0.274	0.238	0.271
	$A_{400\ nm}$ / $A_{640\ nm}$ **Ratio**	1.257	1.358	1.302	1.065	1.382	1.101

5. Discussion

The proposed multiplexers, namely by increasing the chamber diameter, successfully achieved the intended mixing and fluid distribution performance indicators (see section 1). Compared with previously reported passive micromixers in literature, the main advantage of the structures here proposed is their simultaneous integration of mixing and three-way fluid distribution under unequal inlet flow rates. While both geometries achieved effective mixing without external actuation (with MI above 80%), the "Tesla-shaped" with 5000 μm diameter chambers configuration provided the best compromise between mixing uniformity and fluid distribution. The better mixing performance observed for this Tesla-shaped geometry is consistent with previous studies, in which Tesla-based structures and their geometrical modifications have been reported to enhance mixing [58,59]. For the "half--moon-shaped" micromixer, the lower mixing performance suggests that extending the full microchannel length and incorporating additional baffles along the channel could improve mixing, as demonstrated in related studies in literature [60–62]. In terms of multiplexing, increasing the reaction chamber diameter to 5000 μm improved the uniformity of the delivered volumes, with CV around or below 10% in "Tesla-shaped" geometry. This is particularly relevant for multiplexed biosensing, where maintaining comparable flow conditions across parallel reaction chambers is essential for reliable and consistent analysis, in agreement with findings from the literature [63–65].

However, some limitations should be acknowledged. These structures remain limited by their dependence on a restricted range of Newtonian test fluids and flow conditions. In the spectrophotometric study, wide absorbance peaks were recorded. However, this analysis was performed as a complement to microscopy observations and outputted volume measurements, with the primary aim of identifying significant differences in the overall spectra among the three outlets of each microchannel, rather than evaluating the optical absorbance of each pigment individually. Also, the dye solutions employed during the experimental evaluation may cause residue accumulation within the microchannels over time, and therefore alternative dye solutions should be considered in future assessments for device characterization. Additionally, occasional air bubble entrapment on mixing structures was also observed, while slightly higher collected volumes and with different coloration were obtained in the central chamber. These aspects, despite not being critical for the proposed device characterization, may be mitigated through further geometry optimization, especially for "half-moon-shaped" microstructure, which exhibited slightly lower mixing efficiency, where increasing the full microchannel length and the number of microstructures along the channel could enhance mixing. Nevertheless, for PoC or biosensing applications, additional studies need to be performed to evaluate the effects of surface interactions on analyte and label immobilization, their accumulation on the microfluidic substrate, and the need for surface functionalization. Furthermore, testing using real biological samples and functionalized reaction chambers, is therefore necessary before assessing performance against fully validated multiplexed diagnostic platforms.

6. Conclusions and future perspectives

This paper reported the development of a microfluidic multiplexer for passive mixing of two fluids, simultaneously capable of driving equal-volume mixture to three reaction chambers under different flow rate ratios. Four multiplexer geometries were investigated in this study, both numerically and experimentally, combining two micromixer designs, "Tesla-shaped" and "half-moon-shaped", with two different reaction chamber configurations, one comprising three 3500 μm diameter chambers and the other three 5000 μm diameter chambers.

Overall, both "Tesla-shaped" multiplexers demonstrated better performance in terms of mixing and fluid distribution than the "half-moon-shaped" geometries. In particular, the "Tesla-shaped" multiplexer with 3500 μm chambers achieved slightly better mixing efficiency, as evidenced by the similar absorbance spectra of the samples collected from the different outlets, especially at higher flow ratios. However, the geometry with 5000 μm chambers exhibited substantially greater distribution uniformity, with more consistent collected volumes across the different outlets and CV between them below or around 10%, making this configuration the most suitable for further implementation in biosensors and PoC devices.

Concerning the "half-moon-shaped" multiplexer designs, these ones did not exhibit a performance as satisfactory as the "Tesla-shaped" geometries in both chamber configurations. Although the device with 3500 μm diameter chambers showed an ideally expected absorbance spectra, suggesting an efficient mixing, significant disparities in collected sample volumes revealed a heterogeneous distribution. Conversely, the geometry with 5000 μm diameter chambers delivered lower mixing performance but improved fluid distribution, as observed on the Tesla-shaped" multiplexer with the same chamber configuration, indicating that increasing the reaction chamber diameter contributes to a better fluid transport.

Future work may include intensity/concentration calibration using solutions with known concentrations to enable a more direct quantitative comparison between numerical and experimental results. Further geometric optimization should focus on reducing air bubble accumulation and on adjusting both the compensation chamber diameter relative

to that of the main chambers and the channel width connecting the compensation and the central chamber, to ensure proper homogenization and uniform distribution of the mixture among the reaction chambers. The microchannels length and number of microstructures could also be optimized to further improve mixing, particularly for the "half-moon-shaped" geometry. These improvements may also include the (bio)functionalization of the reaction chambers for parallel and simultaneous detection of biomarkers and real-sample testing. Consequently, it will be possible, in a near future, to validate the applicability of the developed device in diagnostic context and to demonstrate its potential for integration into lab-on-a-chip systems.

CRediT authorship contribution statement

Filipe Ferreira: Writing – original draft, Methodology, Investigation, Data curation, Conceptualization. **Paulo J. Sousa:** Writing – review & editing, Validation, Methodology, Investigation, Formal analysis. **Graça Minas:** Writing – review & editing, Validation, Resources, Methodology. **Rui A. Lima:** Writing – review & editing, Validation, Supervision, Resources, Methodology. **Vânia C. Pinto:** Writing – review & editing, Validation, Supervision, Methodology, Funding acquisition, Formal analysis, Conceptualization. **Susana O. Catarino:** Writing – review & editing, Validation, Supervision, Software, Resources, Project administration, Methodology, Funding acquisition, Formal analysis, Conceptualization.

Declaration of competing interest

The authors declare that they have no known competing financial interests or personal relationships that could have appeared to influence the work reported in this paper.

Acknowledgements

This work has been financially supported by the CardioSensing project (COMPETE2030-FEDER-00689800), reference 2023.16645. ICDT (DOI: 10.54499/2023.16645.ICDT), co-financed by European Regional Development Fund (FEDER) and national funds, through Fundação para a Ciência e a Tecnologia (FCT, I.P.), through the Innovation and Digital Transition Programme – Compete2030. The authors acknowledge the partial support of the project 2022.06207.PTDC (DOI: 10.54499/2022.06207.PTDC) co-financed by FEDER and national funds, through FCT, I.P., through the Innovation and Digital Transition Programme – Compete2030; and the project OoCDOXSens (2024.05146.RESTART) founded by FCT, I.P. The authors also acknowledge the FCT partial financial support within the R&D Unit Project Scope: UIDB/04436/2025 (DOI: 10.54499/UID/04436/2025), UID/04077/2025; UID/00532/2025 and LA/P/0045/2020. Paulo Sousa and Vânia Pinto thank FCT for their contracts funding provided through 2021.01086.CEECIND (DOI: 10.54499/2021.01086.CEECIND/CP1664/CT0008) and 2021.01087.CEECIND (DOI: 10.54499/2021.01087.CEECIND/CP1664/CT0020), respectively. The authors declare no conflict of interest.

Supplementary materials

Supplementary material associated with this article can be found, in the online version, at doi:10.1016/j.rineng.2026.113345.

Data availability

Data will be made available on request.

References

[1] V. Mazzaracchio, F. Arduini, Smart microfluidic devices integrated in electrochemical point-of-care platforms for biomarker detection in biological fluids, Anal. Bioanal. Chem. 418 (2) (2026) 459–481, https://doi.org/10.1007/s00216-025-06127-0.
[2] F. Alghannam, et al., Recent progress in PDMS-based microfluidics toward integrated organ-on-a-chip biosensors and personalized medicine, Biosensors 15 (2) (2025) 76, https://doi.org/10.3390/bios15020076.
[3] A. Kazan, Supercritical CO2 applications in microfluidic systems, Microfluid. Nanofluidics. 26 (9) (2022) 68, https://doi.org/10.1007/s10404-022-02574-8.
[4] H. Cai, D. Wang, Y. Zhao, C. Yang, Recent advances in microfluidic chip technology for laboratory medicine: innovations and artificial intelligence integration, Biosensors 16 (2) (2026) 104, https://doi.org/10.3390/bios16020104.
[5] S. Regmi, C. Poudel, R. Adhikari, K.Q. Luo, Applications of microfluidics and organ-on-a-chip in cancer research, Biosensors 12 (7) (2022) 459, https://doi.org/10.3390/bios12070459.
[6] K. Fibben, E.K. Williams, J.D. Roback, W.A. Lam, D.N. Alter, From lab-on-a-chip to lab-on-a-chip-in-the-lab: a perspective of clinical laboratory medicine for the microtechnologist, Lab. Chip. 25 (11) (2025) 2566–2577, https://doi.org/10.1039/D4LC00614C.
[7] B. Gupte, U. Jadhav, S. Gosavi, S. Jagtap, Lab on chip for medical and clinical applications, Sens. Diagn. 4 (11) (2025) 939–965, https://doi.org/10.1039/D5SD00096C.
[8] U.A. Gurkan, et al., Next generation microfluidics: fulfilling the promise of lab-on-a-chip technologies, Lab. Chip. 24 (7) (2024) 1867–1874, https://doi.org/10.1039/D3LC00796K.
[9] R. Kumar, R. Lakkaraju, A. Atta, Inertial flow dynamics and energy dissipation in asymmetrical converging–diverging microchannels: A computational study, Can. J. Chem. Eng. 104 (2) (2026) 1022–1038, https://doi.org/10.1002/cjce.70041.
[10] R.L. Navaei and H. Tehrani, "An integrated lab on a CD microfluidic platform for high-efficiency blood cell separation and passive mixing," 2025.
[11] M. Nouri, S. Ebrahimi, A. Bahramian, A. Dehghan, E. Pishbin, Enhancing circulating tumor cells separation with integrated spiral and U-shaped cross-section microchannels using elasto-inertial microfluidics, Sens. Actuators Phys. 382 (2025) 116153, https://doi.org/10.1016/j.sna.2024.116153.
[12] A.-K. Klein and A. Dietzel, "A primer on microfluidics: from basic principles to microfabrication," 2020, pp. 17–35. doi: 10.1007/10_2020_156.
[13] D. Soltani, T. Persoons, S. Alimohammadi, Fluid dynamics of a microfluidic micromixer–micropump driven by adjacent micro synthetic jets, Int Commun Heat Mass Transf 176 (2026) 111400, https://doi.org/10.1016/j.icheatmasstransfer.2026.111400.
[14] R.R. Gidde, A.P. Kene, B. Mondal, Numerical analysis of mixing performance in micromixers with chambers and baffles for mixing applications, Microsyst. Technol. 31 (11) (2025) 3281–3298, https://doi.org/10.1007/s00542-025-05929-7.
[15] P.B. Flandrin, et al., Comparative study of State-of-the-art micromixers: mixing efficiency and design recommendations, Adv. Eng. Mater. (2026) e71123, https://doi.org/10.1002/ADEM.71123;CSUBTYPE:STRING:AHEAD.
[16] T.A. Shitab, A. Ibnat Oni, M.E. Hossain Emon, R. Rayan Rahat, A.A. Mim, P. Fariya Auishe, Microfluidic Simulation Framework for point-of-care diagnostics: modeling advection-diffusion-reaction transport in lab-on-chip systems, in: 2025 IEEE International Conference on Biomedical Engineering, Computer and Information Technology for Health, BECITHCON 2025, 2025, pp. 747–751, https://doi.org/10.1109/BECITHCON69222.2025.11504301.
[17] R. Karnik, Microfluidic mixing. Encyclopedia of Microfluidics and Nanofluidics, Springer New York, New York, NY, 2015, pp. 1969–1979, https://doi.org/10.1007/978-1-4614-5491-5_939.
[18] J. Castillo-León, W.E. Svendsen (Eds.), Lab-on-a-Chip Devices and Micro-Total Analysis Systems, Springer International Publishing, Cham, 2015, https://doi.org/10.1007/978-3-319-08687-3.
[19] H. Shang, C. Xu, Passive single-chamber micromixer with high throughput and low-pressure drop, Ind. Eng. Chem. Res. 64 (31) (2025) 15449–15463, https://doi.org/10.1021/acs.iecr.5c00965.
[20] M. Bayareh, M.N. Ashani, A. Usefian, Active and passive micromixers: A comprehensive review, Chem. Eng. Process - Process Intensif. 147 (2020) 107771, https://doi.org/10.1016/j.cep.2019.107771.
[21] S. Faraji, J.R. Shahrouzi, Comprehensive experimental and numerical investigation of a microrod-based active micromixer driven by the magnetic stirring mechanism, J. Taiwan. Inst. Chem. Eng. 173 (2025) 106160, https://doi.org/10.1016/j.jtice.2025.106160.
[22] M. Li, Y. Chen, G. Yang, S. Li, C. Wu, C. Xiang, A numerical and experimental study of an efficient micromixer at low reynolds number using vibration signal, Chem. Eng. Res. Des. 221 (2025) 444–460, https://doi.org/10.1016/j.cherd.2025.08.029.
[23] M. Wang, et al., A micromixer actively driven by micro-thin piezo pumps, Int. J. Mech. Sci. 321 (2026) 111656, https://doi.org/10.1016/j.ijmecsci.2026.111656.
[24] W. Han, W. Li, H. Zhang, A comprehensive review on the fundamental principles, innovative designs, and multidisciplinary applications of micromixers, Phys. Fluids 36 (10) (2024), https://doi.org/10.1063/5.0238393.
[25] C.-Y. Lee, W.-T. Wang, C.-C. Liu, L.-M. Fu, Passive mixers in microfluidic systems: A review, Chem. Eng. J. 288 (2016) 146–160, https://doi.org/10.1016/j.cej.2015.10.122.

[26] B. Talebjedi, M. Ghazi, N. Tasnim, S. Janfaza, M. Hoorfar, Performance optimization of a novel passive T-shaped micromixer with deformable baffles, Chem. Eng. Process - Process Intensif. 163 (2021) 108369, https://doi.org/10.1016/j.cep.2021.108369.
[27] J.-C. Hsu, Enhanced micromixing using surface acoustic wave devices: fundamentals, designs, and applications, Micromachines 16 (6) (2025) 619, https://doi.org/10.3390/mi16060619.
[28] A.M.K. Abhilash, A.S. Kumar, J.S. Babu, Advances in passive micromixer designs for biochemical systems: A review on mechanistic insights and performance evaluation, Chem. Eng. J. Adv. 26 (2026) 101122, https://doi.org/10.1016/j.ceja.2026.101122.
[29] S.R. Bazaz, A. Sayyah, A.H. Hazeri, R. Salomon, A.A. Mehrizi, M.E. Warkiani, Micromixer research trend of active and passive designs, Chem. Eng. Sci. 293 (2024) 120028, https://doi.org/10.1016/j.ces.2024.120028.
[30] M. Juraeva, D.-J. Kang, Design and analysis of a passive micromixer based on multiple passages, Micromachines 16 (5) (2025) 592, https://doi.org/10.3390/mi16050592.
[31] E. bennour, N. Kaid, A. Mouissi, Numerical investigation on a chaotic passive micromixer based on square chambers connected with different channel shapes for enhancing the mixing process, Ind. Eng. Chem. Res. 63 (6) (2024) 2861–2874, https://doi.org/10.1021/acs.iecr.3c03567.
[32] W. Raza, S. Hossain, K.-Y. Kim, A review of passive micromixers with a comparative analysis, Micromachines 11 (5) (2020) 455, https://doi.org/10.3390/mi11050455.
[33] F. Ferreira, P.J. Sousa, G. Minas, R.A. Lima, V.C. Pinto, S.O. Catarino, Numerical and experimental analysis of mixing efficiency in passive micromixers under laminar flow, in: 2025 IEEE 8th Portuguese Meeting on Bioengineering (ENBENG), IEEE, 2025, pp. 21–24, https://doi.org/10.1109/ENBENG67130.2025.11199608.
[34] T. Thienthong, et al., Mixing-performance evaluation of a multiple dilution microfluidic chip for a Human serum dilution process, Eng. J. 25 (9) (2021) 67–87, https://doi.org/10.4186/ej.2021.25.9.67.
[35] B. Yuan, S. Yuan, H. Wang, Numerical and experimental investigation of mixing enhancement in a zigzag passive micromixer with D-shaped obstacles, Micromachines 17 (2) (2026) 190, https://doi.org/10.3390/mi17020190.
[36] M. Juraeva, D.-J. Kang, Design and mixing analysis of a passive micromixer with circulation promoters, Micromachines 15 (7) (2024) 831, https://doi.org/10.3390/mi15070831.
[37] J. Li, B. Ma, X. Zhang, Q. Zhao, R. Sun, J. Zhao, Design and optimization of Tesla micromixer with asymmetrical arrangement for efficient mixing in microfluidic chip, Chem. Eng. Process - Process Intensif. 209 (2025) 110181, https://doi.org/10.1016/j.cep.2025.110181.
[38] Y. Geng, et al., Design and research of a passively mixed microfluidic chip for copper ion detection, PLoS. One 21 (2) (2026) e0343203, https://doi.org/10.1371/journal.pone.0343203.
[39] B. Liu, et al., Portable, facile microfluidic platform using a low-cost vacuum pump for multiplex biomarker detection in human samples, Sens. Actuators. B Chem. 426 (2025) 136994, https://doi.org/10.1016/j.snb.2024.136994.
[40] C. Wang, et al., Multiplexed immunosensing of cancer biomarkers on a split-float-gate graphene transistor microfluidic biochip, Lab. Chip. 24 (2) (2024) 317–326, https://doi.org/10.1039/D3LC00709J.
[41] J. Li, et al., Simultaneous detection of multiple Respiratory pathogens using an integrated microfluidic chip, Anal. Chem. (2024), https://doi.org/10.1021/acs.analchem.4c00990.
[42] P. Punnoy, et al., Smartphone-assisted dual-sided capillary microfluidic device for multiplex detection of heavy metals and nutrients in drinking water, Anal. Chim. Acta 1356 (2025) 344031, https://doi.org/10.1016/j.aca.2025.344031.
[43] F. Liu, et al., A multi-channel microfluidic chip based on fluorescent distance readout-mode for rapid, simultaneous and visual detection of multiplex pathogens using phage- AIEgen-antimicrobial peptide-encoded tags, Sens. Actuators. B Chem. 424 (2025) 136867, https://doi.org/10.1016/j.snb.2024.136867.
[44] E. Osman, J. L'Heureux-Hache, P. Li, L. Soleymani, Design and simulation of biomimetic microfluidic designs to achieve uniform flow and DNA capture for high-throughput multiplexing, Lab. Chip. 25 (6) (2025) 1462–1473, https://doi.org/10.1039/D4LC01023J.
[45] J. Peng, et al., A microfluidic-based chemiluminescence biosensor for sensitive multiplex detection of exosomal microRNAs based on hybridization chain reaction, Talanta 281 (2025) 126838, https://doi.org/10.1016/j.talanta.2024.126838.
[46] D.H. Han, et al., Pushbutton-activated microfluidic cell-free biosensor for multiplexed pathogen detection, Lab. Chip. 25 (22) (2025) 5950–5960, https://doi.org/10.1039/D5LC00337G.
[47] S.O. Catarino, P. Felix, P.J. Sousa, V. Pinto, M.I. Veiga, G. Minas, Portable device for optical quantification of hemozoin in diluted blood samples, IEEE Trans. Biomed. Eng. 67 (2) (2020) 365–371, https://doi.org/10.1109/TBME.2019.2913454.
[48] M.O. Correia, P. Sousa, R.O. Rodrigues, G. Minas, A proof-of-concept study aiming for the integration of an optical biosensor in advanced microfluidic devices for Alzheimer's Disease studies, Appl. Sci. 15 (7) (2025) 3837, https://doi.org/10.3390/app15073837.
[49] S. Hossain, M.A. Ansari, A. Husain, K.-Y. Kim, Analysis and optimization of a micromixer with a modified Tesla structure, Chem. Eng. J. 158 (2) (2010) 305–314, https://doi.org/10.1016/j.cej.2010.02.002.
[50] T. Dehghani, F. Sadegh Moghanlou, M. Vajdi, M. Shahedi Asl, M. Shokouhimehr, M. Mohammadi, Mixing enhancement through a micromixer using topology optimization, Chem. Eng. Res. Des. 161 (2020) 187–196, https://doi.org/10.1016/j.cherd.2020.07.008.
[51] F. Aksoy, G. Yesiloz, Enhanced microfluidics mixing performance in a grooved serpentine microchannel at different flow rates, Celal Bayar Üniversitesi Fen Bilimleri Dergisi 19 (3) (2023) 253–260, https://doi.org/10.18466/cbayarfbe.1293522.
[52] D. Li, et al., The butterfly effect of tiny density difference in microfluidic channel, Int. J. Mech. Sci. 300 (2025) 110430, https://doi.org/10.1016/j.ijmecsci.2025.110430.
[53] N. Bannach, "Characterizing the flow and choosing the right interface." Accessed: Jul. 18, 2024. [Online]. Available: https://www.comsol.com/blogs/characterizing-flow-choosing-right-interface.
[54] "Users Guide Comsol Multiphysics ®." [Online]. Available: www.comsol.com/support/knowledgebase.
[55] M. Waqas, A. Palevicius, V. Jurenas, K. Pilkauskas, G. Janusas, Design and investigation of a passive-type microfluidics micromixer integrated with an Archimedes screw for enhanced mixing performance, Micromachines 16 (1) (2025) 82, https://doi.org/10.3390/mi16010082.
[56] V. Pinto, P. Sousa, V. Cardoso, G. Minas, Optimized SU-8 processing for low-cost microstructures fabrication without cleanroom facilities, Micromachines 5 (3) (2014) 738–755, https://doi.org/10.3390/mi5030738.
[57] H. Fu, X. Liu, S. Li, Mixing indexes considering the combination of mean and dispersion information from intensity images for the performance estimation of micromixing, RSC. Adv. 7 (18) (2017) 10906–10914, https://doi.org/10.1039/C6RA23783E.
[58] M. Juraeva, D.-J. Kang, Mixing performance of the modified Tesla micromixer with tip clearance, Micromachines 13 (9) (2022) 1375, https://doi.org/10.3390/mi13091375.
[59] B. Abolpour, R. Hekmatkhah, R. Shamsoddini, Optimum design for the Tesla micromixer, Microfluid. Nanofluidics. 26 (6) (2022) 46, https://doi.org/10.1007/s10404-022-02530-6.
[60] W. Wang, M. Li, C. Xu, Selective scaling-out of a serpentine micromixer: scaling criteria, Ind. Eng. Chem. Res. 63 (5) (2024) 2374–2383, https://doi.org/10.1021/acs.iecr.3c03604.
[61] P. Flandrin, et al., Comparative study of State-of-the-art micromixers: mixing efficiency and design recommendations, Adv. Eng. Mater. (2026), https://doi.org/10.1002/adem.71123.
[62] Q. Fu, Z. Liu, S. Cao, Z. Wang, G. Liu, Topology-optimized micromixer design with enhanced reverse flow to increase mixing efficiency, Micromachines 14 (8) (2023) 1599, https://doi.org/10.3390/mi14081599.
[63] S. Kramer et al., "A handheld microfluidic manifold for massively multiplexed nucleic acid detection," 2025. doi: 10.1101/2025.08.11.669785.
[64] A.R. Vollertsen, et al., Highly parallelized human embryonic stem cell differentiation to cardiac mesoderm in nanoliter chambers on a microfluidic chip, Biomed. Microdevices 23 (2) (2021) 30, https://doi.org/10.1007/s10544-021-00556-1.
[65] M. Khalghollah, A. Zare, S. Abdollahi, B.H. Far, A. Sanati Nezhad, Machine learning-driven capillary microfluidic design automation for programmable gradient generation and antimicrobial testing, Small 22 (37) (2026), https://doi.org/10.1002/smll.73821.